Potential Pitfalls in the Analysis and Structural Interpretation of Seismic Data from the Mars InSight Mission

Doyeon Kim, Paul Davis, Ved Lekić, Ross Maguire, Nicolas Compaire, Martin Schimmel, Eleonore Stutzmann, Jessica C. E. Irving, Philippe Lognonné, John-Robert Scholz, et al.

To cite this version:

Doyeon Kim, Paul Davis, Ved Lekić, Ross Maguire, Nicolas Compaire, et al.. Potential Pitfalls in the Analysis and Structural Interpretation of Seismic Data from the Mars InSight Mission. Bulletin of the Seismological Society of America, 2021, 10.1785/0120210123 . hal-03390358

HAL Id: hal-03390358

https://hal.science/hal-03390358v1

Submitted on 23 Sep 2023

Potential Pitfalls in the Analysis and Structural Interpretation of Seismic Data from the Mars InSight Mission

D. Kim[1*], P. Davis[2], V. Lekić[1], R. Maguire[1,3], N. Compaire[4], M. Schimmel[5], E. Stutzmann[6], J.C.E. Irving[7], P. Lognonné[6], J.-R. Scholz[8], J. Clinton[9], G. Zenhäusern[10], N. Dahmen[10], S. Deng[11], A. Levander[11], M. Panning[12], R. F. Garcia[4], D. Giardini[10], K. Hurst[12], B. Knapmeyer-Endrun[13], F. Nimmo[14], W. T. Pike[15], L. Pou[14], N. Schmerr[1], S. C. Stähler[10], B. Tauzin[16], R. Widmer-Schnidrig[17], W. B. Banerdt[12]

Affiliations:

1. Department of Geology, University of Maryland, College Park, MD, USA
2. Department of Earth, Planetary and Space Sciences, University of California, Los Angeles, CA, USA
3. Department of Computational Mathematics, Science, and Engineering, Michigan State University, East Lansing, MI, USA
4. Institut Supérieur de l'Aéronautique et de l'Espace SUPAERO, Toulouse, France
5. Geosciences Barcelona – CSIC, Barcelona, Spain
6. Université de Paris, Institut de Physique du Globe de Paris, CNRS, Paris, France
7. School of Earth Sciences, University of Bristol, Bristol, UK
8. Max Planck Institute for Solar System Research, Göttingen, Germany
9. Swiss Seismological Service (SED), ETH Zürich, Zürich, Switzerland
10. Institute of Geophysics, ETH Zürich, Zürich, Switzerland
11. Department of Earth, Environmental and Planetary Sciences, Rice University, Houston, TX, USA
12. Jet Propulsion Laboratory, California Institute of Technology, Pasadena, CA, USA.
13. Bensberg Observatory, University of Cologne, Bergisch Gladbach, Germany.

14. Department of Earth and Planetary Sciences, University of California Santa Cruz, Santa Cruz, CA, USA

15. Department of Electrical and Electronic Engineering, Imperial College London, London, UK

16. Université de Lyon, Laboratoire de Géologie de Lyon: Terre, Planètes, Environnement, Villeurbanne, France.

17. Black Forest Observatory, Institute of Geodesy, University of Stuttgart, Stuttgart, Germany

*Correspondence to: Doyeon Kim (dk696@cornell.edu)

Conflict of interest

The authors acknowledge there are no conflicts of interested recorded.

Abstract

The Seismic Experiment for Interior Structure (SEIS) of the *InSight* mission to Mars, has been providing direct information on Martian interior structure and dynamics of that planet since it landed. Compared to seismic recordings on Earth, ground motion measurements acquired by SEIS on Mars are made under dramatically different ambient noise conditions, but include idiosyncratic signals that arise from coupling between different *InSight* sensors and spacecraft components. This work is to synthesize what is known about these signal types, illustrate how they can manifest in waveforms and noise correlations, and present pitfalls in structural interpretations based on standard seismic analysis methods. We show that glitches, a type of prominent transient signal, can produce artifacts in ambient noise correlations. Sustained signals that vary in frequency, such as lander modes which are affected by variations in temperature and wind conditions over the course of the Martian Sol, can also contaminate ambient noise results. Therefore, both types of signals have the potential to bias interpretation in terms of subsurface layering. We illustrate that signal processing in the presence of identified nonseismic signals must be informed by an understanding of the underlying physical processes in order for high fidelity waveforms of ground motion to be extracted. While the origins of most idiosyncratic signals are well understood, the 2.4 Hz resonance remains debated and the literature does not contain an explanation of its fine spectral structure. Even though the selection of idiosyncratic signal types discussed in this paper may not be exhaustive, we provide guidance on best practices for enhancing the robustness of structural interpretations.

Introduction

Measurements of ground vibrations recorded by seismometers enable imaging of our planet's inaccessible interior and provide information about processes below and above its surface. Seismologists have developed many techniques for extracting structural signals from waveforms of ground vibrations, many of which require high fidelity recordings. Recently, methods based on autocorrelation have particularly grown in prominence (e.g. Ito & Shiomi, 2012; Gorbatov et al., 2013; Pham & Tkalčić, 2017; Romero & Schimmel, 2018; Kim et al., 2019a). Modern broadband seismometers are designed to measure ground motions to a tenth of a typical atomic spacing between two bonded atoms. Because of this remarkable sensitivity, signals influenced by physical structures and processes in the subsurface are recorded alongside ground vibrations generated by unrelated processes, including ocean waves (e.g., Longuet-Higgins, 1950; Webb, 2007), wind (e.g., Dybing et al. 2019), earth tides (e.g., Martynov et al. 2020), cultural noise (e.g., Quiros et al., 2016; Lecocq et al., 2020), and even variations of the Earth's magnetic field (e.g., Forbriger, 2007, Tape et al., 2020).

The Seismic Experiment for Interior Structure (SEIS) contains two independent 3-component seismometers, a miniature Short Period (SP) and a Very Broad Band (VBB) sensor (Lognonné et al., 2019). SEIS-VBB has greater sensitivity at low frequencies, equal to that of observatory-class instruments deployed on Earth (Lognonné et al., 2019), but the ambient noise level at frequencies of 0.2 - 1 Hz is approximately 500 times lower than the Earth's microseismic noise (Lognonné et al., 2020). The VBB instrument is one of many electro-mechanical components of the spacecraft system of the *InSight* Mission (Banerdt et al., 2020) interconnected to the lander which also includes the Heat Flow and Physical Properties Package (HP^3, Spohn et al., 2018), a radio transponder to track rotation of Mars (Folkner et al., 2018), and other environmental monitoring sensors (Banfield et al., 2019).

Just as one may be able to hear a watch ticking in a quiet room, *InSight's* seismic data permit us to "listen" to various sensors and the mechanical components of the spacecraft system "talking" to each other during the quiet period of the Martian day (roughly between 17:00 and 22:00 Local Mean Solar Time, LMST for ½ the martian year centered around InSights' summer). We can also hear signals due to winds (Suemoto et al., 2020; Charalambous et al., 2020; Stutzmann et al., 2021), as well as the lander itself. Due to the high sensitivity of the VBB seismometer, the complexities associated with the coupling of different lander components under relatively underexplored environmental conditions, and the low ambient noise levels, the seismic data being collected on the surface of Mars contains several idiosyncratic signals that are not normally found on seismometers on the Earth or the Moon (e.g., Latham et al., 1970) and more similar to signals from ocean bottom seismometers (e.g., Sutton et al. 1981; Stähler et al. 2016). Furthermore, there are other peculiarities in seismograms whose origin is not yet fully understood.

Figure 1 presents an overview of the SEIS VBB ground vibration recordings during a typical Martian Sol (Sol 184, 2019-06-03UTC 06:00 – 2019-06-04UTC 08:00). In addition to the long period features associated with variations in wind conditions (Lognonné et al., 2020; Stutzmann et al., 2021), various types of short period resonances and other nonseismic signals are also apparent in both time and frequency domains (Fig. 1A-E). Based on the signal duration, two types of peculiar signals exist: transient and sustained signals (illustrated on both Figs. 1C and E). These idiosyncratic signals are routinely identified by the Marsquake Service (MQS, Clinton et al., 2018) who promptly checks all data arriving from Mars and can be further classified.

Transient signals in SEIS data are described as follows:

i) One of the most prominent and numerous types of transient signals is referred to as "*glitch*" that is represented by a step function in acceleration convolved with instrument response (Scholz et al., 2020). The large majority of glitches are either due to (1) the relaxation of the suspension spring (causing glitches only on a single component) or (2) an internal deformation and subsequent tilting of the VBB sensor or the whole sensor assembly (causing multi-component glitches; e.g., Fig. 1H). The origin of such tilting remains debated and possible mechanisms are discussed in more detail by Scholz et al. (2020).

ii) Glitches are often preceded by a high frequency precursor, referred to as "*spike*"; however, spikes can occur without glitches. These spike signals can have either the same or the opposite polarity as the glitches (e.g., Fig. 1H) and they are interpreted as arising from a step function in displacement (Scholz et al., 2020; Ceylan et al., 2020);

iii) The third type of transient signal artifacts that are usually only visible at high frequencies (>10 Hz) are referred to as "*donks*" and are typically observed on all three components (e.g., inset, Fig. 1F). These are rarely visible in the continuous 20 sample per second (sps) data;

Due to the large diurnal temperature variations on Mars (e.g., Banfield et al., 2020), the interconnected mechanical components of the *InSight* spacecraft periodically release thermoelastic stresses giving rise to these short duration signals recorded by the seismometer (Scholz et al., 2020; Ceylan et al., 2020). Compared to terrestrial settings, it is important to state that these glitches are neither fully randomly distributed in time, as in ageing seismometers (e.g., Wielandt, 2012), nor periodic, as in certain ocean-bottom seismometers (e.g., Stähler et al. 2016; Deen et al. 2017).

Sustained signals in SEIS data are described as follows:

i) *The lander modes* – mechanical resonances of the *InSight* spacecraft system (e.g. Murdoch et al. 2018) – show up as several prominent peaks in the frequency domain (e.g., 3.3 Hz, 4.1 Hz, 6.8 Hz, and 8.6 Hz; Fig. 1C and 1E). Observations from the short period (SP) seismometer on-deck of the lander and those from the Martian surface after deployment show consistent behavior of the lander modes, and have shown that their frequency varies with temperature and windspeed (Panning et al., 2020; Clinton et al., 2021; Dahmen et al., in review). This is similar to observations of resonant modes in ocean-bottom seismometers (e.g., Trehu, 1985; Stähler et al. 2018);

ii) A narrow-band sustained artifact at 1 Hz is referred to as a "*tick*" and can be seen in the frequency domain alongside its higher harmonics up to 6 Hz (Fig. 1I-J). This signal is due to electrical cross-talk produced by the SEIS temperature measurements where the EBOX on the lander interrogates the temperature sensors inside SEIS once every second (Ceylan et al., 2020; Zweifel et al., 2021); During the commissioning phase, the temperature sensors were sampling once every 10s resulting in tick noise at 0.1 Hz and the corresponding harmonics. For a schematic overview of the VBB and its subsystem configuration, see Fig. 33 in Lognonné et al. (2019).

iii) The sustained peculiarity showing a broad and complicated spectral peak near 2.4 Hz is simply referred to as the "*2.4 Hz resonance*." Its energy (Fig. 1C and 1E) is more pronounced relative to background noise during the quiet period of the Martian Sol. The origin of the signal remains unclear and is being investigated under two working hypotheses: the resonance is either being generated by seismic energy reverberating within the subsurface structure beneath the lander (e.g., Giardini et al., 2020; Pan et al., 2020) or by resonances of the lander solar panels (for a schematic of the solar panel configuration, see Fig. 1 in Ceylan et al., 2020).

The aim of this work is to illustrate how these idiosyncrasies of Martian seismic data can manifest in waveforms and noise correlograms, and to provide guidance for making robust structural interpretation. Because the spectral content of these transient and sustained signals spans the range of frequencies used by diverse seismological techniques for structural interpretations, extra scrutiny of data is needed when computing noise correlograms (e.g., Compaire et al., 2021; Schimmel et al., 2021), receiver functions (e.g., Knapmeyer-Endrun et al., 2021) or identifying seismic phases from marsquakes (e.g., Khan et al. 2021; Stähler et al., 2021). Without this added scrutiny, interpretation of Martian structure from the regolith through crustal and mantle layering to core structure could be impeded. The manuscript is organized into five sections called pitfalls, each of which outline the overall characteristics of a particular waveform artifact, and how they can potentially contaminate the data and hence lead to an inaccurate interpretation of the Martian structure.

Pitfall 1: Effect of Glitches

Several methods have been devised to remove glitches from raw SEIS-VBB data. The performance of these methods is reliable and sensitive down to 10^{-8} m/s in amplitude (see Scholz et al., 2020 for different glitch removal algorithms). To illustrate how glitches manifest in the SEIS-VBB data and how these signals manifest themselves in a standard ambient noise processing framework, we preprocess continuous recordings of the ambient noise on Mars between February and July, 2019. We take the raw 20 sps UVW channels from SEIS-VBB, remove the instrument transfer function through spectral division, and rotate to ZNE components. The three-component data is then segmented into a total of 1051 two-hour-long records. We then apply a "deglitching" algorithm to obtain three types of datasets: 1) vertical component data which only contains identified glitch signals (Fig. 2); 2) raw vertical component data with glitches; 3) vertical component data with glitches removed.

A first step in standard seismic data processing involves removal of the seismometer's transfer function which converts the raw counts into a physical unit of ground motion. When this operation is performed on a glitch waveform, two potential issues may occur. First, because the glitch in the raw data represents a step function in acceleration caused by tilts, treating it as a translational motion is inappropriate. This is because the glitch signal in the SEIS-VBB data converted to either velocity or displacement by the subsequent integration of the acceleration step would lead to a ramp in velocity or a parabola in displacement which of course are nonphysical because a linearly increasing velocity with time would imply that the SEIS system would have left the surface of mars shortly after the glitch occurred. For this reason, we label the velocity and displacement traces in Fig 2D as pseudo velocity and pseudo displacement. Second, depending on the choice of the filter used while implementing instrument removal, processing artifacts can be generated. For example, the instrument-removed glitch in acceleration shown in Fig. 2D (dashed red) is the resulting signal processed by a commonly used module, ObsPy (Beyreuther et al., 2010) in the Python programming language. An acausal, zero-phase filter is applied here to the glitch by spectral division within a limited frequency band. This is a common but not necessarily optimal method because the instrument-removed glitch now shows a trend superimposed on the step function. If one wishes to retrieve the physically correct representation of the glitch in acceleration (Fig 2E), the response of the VBB system and its corresponding recursive filter constants (e.g., Wielandt and Streckeisen, 1982) need to be estimated more carefully (e.g., Kanamori and Rivera, 2008; Anderson and Lees, 2014) to preserve causality. Careful consideration of how standard signal processing flows can lead to waveform distortion in the presence of glitches is also highlighted in the strong motion literature (e.g., Boore and Bommer, 2005).

Further signal analysis may involve identifying and removing the glitches. We use two approaches to identify glitches and compare their performance. In the first approach, we start by decimating the 20 sps vertical component data to 2 sps to improve the computational efficiency and minimize the spikes in the raw data (see Pitfall 2). For each 2-hour record (between February and July 2019), we identify peaks with a signal-to-noise ratio in their vicinity greater than 4. We then perform template matching by cross-correlating data segments around the times of the peaks with the response-removed (acausal) glitch template (e.g., blue, Fig. 2D). For peaks spaced closely in time, we use a series of templates. We define the signal as a glitch if the correlation coefficient exceeds 0.9 and mark it on the corresponding 20 Hz data (e.g., orange lines, Fig. 2B). The second approach (Scholz et al., 2020) also starts by decimating the data, but seeks to identify glitches directly from the UVW channels. Instrument response is removed to obtain accelerograms, so that the physical model for the glitches -- which manifest as steps in acceleration (e.g., Fig 2E) -- can be exploited for detection. A time-derivative of the accelerograms results in a spike at each glitch, which are identified when they exceed a threshold value. The latter approach is applied to 2-hour records with a different recording time span between March and September, 2019. Both deglitching methods removed the bulk of the glitch energy, but not all, and some overfitting occurs when threshold levels are set too low (see Fig. 2B). However, the conclusions regarding the effect of glitches on noise correlograms remained the same in either case.

To estimate the percentage of contamination due to glitches present in our data, we compute the Hilbert envelope for each glitch-only record (e.g., orange, 2B), select amplitudes larger than a threshold value set at 0.25% of the maximum, and generate a binary mask. We estimate that setting a lower threshold value would only result in <1% difference for the estimate of the percentage of contamination. We find that a significant portion of our data is affected by glitches (Fig. 2A). For each 2-hr segment, the percentage of contamination due to glitches coherently fluctuates with the Martian diurnal noise cycle (e.g., Lognonné et al., 2020) and the value increases up to 74% especially during the quiet period of the Martian Sol. Often contamination by glitches is consistently observed across the entire 2-hour span of our data and the percentage value periodically rises up to 37% (Fig. 2A). This implies that these temperature-driven signals (Scholz, et al., 2020) may be stationary (e.g., Barkaoui et al., 2019) though a complete analysis on glitches is being hindered by the strong wind noise during the noisy period on Mars (daytime, Fig. 1; Fig. 2B).

To assess the effect of acausal glitches on noise correlation functions, we compute autocorrelation functions (ACFs) using vertical component data that consists only of glitch signals identified between February – July, 2019 (i.e., Dataset 1). We apply 1-bit normalization to our data prior to autocorrelation, which is a standard way of implementing spectral whitening in analyses of ambient noise recordings on Earth (e.g., Shapiro et al., 2005). Following Deng and Levander (2020), we analyze our ACFs in two frequency ranges: high frequency (HF, 0.625 – 2.5 Hz) and low frequency (LF, 0.05 – 0.1 Hz).

We find that individual ACFs produced by correlating each 2-hour glitch segment show many coherent arrivals in both HF and LF ACFs (Fig. 3). The timings of these arrivals are more pronounced in the ACF stacks as we sum all the individual ACFs performed in a phase-weighted fashion (Schimmel and Paulssen, 1997). As expected, the strongest arrivals in our ACF stacks originate from a glitch signal being correlated by itself. Because of the symmetrical shape of the deconvolved glitch in velocity (blue, Fig. 2D), their corresponding signal widths and sidelobes give rise to a few stationary phases (e.g., Snieder, 2004) during the process of autocorrelation. For example, the 60s duration of the glitch signal (reciprocal in frequency ~ 0.0167 Hz) in pseudo-velocity bandpass filtered between 0.01 – 8 Hz (see inset, Fig. 3C), produces coherent arrivals in the autocorrelation at lag-times ~30 and ~60s (Fig. 3A). Moreover, the detailed timings of these arrivals can vary and one may expect various other arrivals since the design of the pre-filter applied during the instrument removal process (Fig. 3A-B) can result in variations in apparent glitch duration. Additional arrivals may arise from systematics in the timing between glitches. But because similar pseudo-velocity glitches persist throughout the SEIS-VBB data and our 2-hour waveform segments are contaminated with those glitches up to 74% of the time (Fig. 2A), the glitch removal process is nevertheless critical to obtain robust ACFs.

Recently, Deng and Levander (2020) used 2-hour segmented ambient noise records and computed ACFs (hereafter DL ACFs) for SEIS-VBB data. They use an ambient noise processing procedure that is well-established and commonly applied to data recorded on Earth (e.g., Sabra et al., 2005; Bensen et al., 2007; Lin et al., 2013; Kim et al., 2019b). To suppress glitches and tick noise in the data, they apply temporal balancing (e.g., Bensen et al., 2007) and two notch filters to reject signals around 1 and 2 Hz (see Pitfall 4). The authors identify at least three major seismic boundaries of Mars from their resulting ACFs. These include two "crustal" phases (i.e., interpreted as P-wave and S-wave reflections from the Moho) observed in the vertical component SP ACFs and the two deeper phases (i.e., P-wave reflections from the olivine to wadsleyite phase transition and core-mantle boundary) in their LP counterparts (Deng and Levander, 2020).

To assess how glitch contamination of actual ground vibrations recorded on Mars by SEIS-VBB, might affect structural interpretation of ACFs like those analyzed by Deng and Levander

(2020), we also compute autocorrelations on raw and deglitched waveforms. We replicate both DL ACFs in HF and LF using raw 2-hour vertical component data (Dataset 2) followed by the ambient noise processing steps in Deng and Levander (2020) including a temporal balancing approach to suppress glitches. The phase-weighted stacks of the individual HF and LF DL ACFs show identical phases at ~11.5s and 21.0s and ~280s and ~375s, respectively as previously documented by those authors. Next, our replicated DL ACFs are benchmarked with another set of ACFs derived from the deglitched waveforms (Dataset 3) obtained by applying the additional glitch removal procedure.

The two phases interpreted as "crustal" reflections are apparent in both HF ACF stacks: raw and glitch-removed data (blue and black, Fig. 4A). Observation of these phases in HF ACFs is also consistent with other noise correlation studies to within a time difference of less than 1s (Compaire et al., 2021; Schimmel et al., 2021; Knapmeyer-Endrun et al., 2021). On the other hand, the HF ACF stack based on our glitch-only waveforms (Dataset 1) did not contain such signals (orange, Fig. 4A). This implies that the duration and spacing of most of the glitches in our HF data stream are well beyond 30s, hence they do not produce spurious signals in the HF ACFs. We find that, surprisingly, these two crustal phases are insensitive to different preprocessing steps employed by Deng and Levander (2020) and this work so that all the HF ACFs produced with and without the data normalization steps (i.e., nonlinear temporal balancing and spectral whitening) have turned out to be virtually identical (Fig. 4C). Further implication for the structural interpretation of crustal phases will be further discussed along with Pitfall 5, the 2.4 Hz resonance.

In contrast to the HF ACF stacks, the LF stacks are inconsistent across our three datasets regardless of the presence of glitches (Fig. 4B). While we successfully replicate the two conspicuous "deep" phases of the DL ACFs in the LF ACF stack using the raw data with glitches

(Dataset 2), the corresponding ACF stack resulting from the glitch-removed waveforms (Dataset 3) fail to reproduce either of those phases. Instead, other later phases are present and they arrive after 375s which is an inconsistent observation relative to the DL LF ACF stack. This time the data normalization step, especially the nonlinear temporal balancing (Bensen et al., 2007), affected the outcome of the LF ACF stacks. Notably, the ~280s phase in DL LF ACF stack disappears without the application of data normalization in time (Fig. 4D). However, this first deep phase is clearly reproduced by applying the complete noise processing flow described in Deng and Levander (2020) with the dataset that only contains glitch signals (orange, Fig. 4B) (Dataset 1). Though relatively attenuated, the ~ 375s phase is weakly observable in the same LF ACF stack produced by glitches (orange, Fig. 4B). On the other hand, the LF ACF stack identically processed using a different glitch-removed noise dataset (2-hour records between March and September, 2019 with glitches identified and removed followed by Scholz et al., 2020) (green, Fig. 4B) verify our finding that the second deep phase is unstable and inconsistent across different datasets. Therefore, we conclude that glitches can substantially affect appearance of ACFs in the lag-time window corresponding to potential mantle transition zone and core reflections; structural interpretations of such deep reflections should be approached with a careful treatment of glitches. Note also, that reflections of interfaces deeper than the Moho have only been observed using noise correlation on Earth by stacking cross-correlations of thousands of station pairs (Lin et al. 2013; Retailleau et al., 2020). On Mars, observation of such a phase is significantly less plausible, given its much lower ambient seismic excitation level, due to the lack of oceans or strong quakes. This example highlights the effect of Pitfall 1 - glitches. Without using properly deglitched waveforms collected by the *InSight* mission (e.g., Scholz et al., 2020), any result from a similar analysis can be heavily contaminated by glitch artifacts, which will depend on the specifics of glitch duration and systematics in glitch separation time. These artifacts can bias interpretation of ACFs, whether the raw data contains ground vibration measurements due to ambient noise or various types of marsquake events.

Pitfall 2: Spikes and donks

As discussed above, glitches in the SEIS-VBB data are modeled as a step function in acceleration resulting from tilt of the sensor assembly. Similarly, spikes (or high frequency precursors to glitches) are modeled as the response to a simultaneous step in displacement, resulting from the associated small vertical movement whose amplitude is proportional to the distance from the tilt axis and the sensor. Indeed, this working hypothesis is directly employed when devising a method to remove glitches in the data stream (Scholz et al., 2020). Because spikes exist at higher frequencies (>1 Hz) than glitches and the majority of spikes are found simultaneously with the glitch onset, the simplest way to identify them is by leveraging existing glitch removal algorithms. Note, however, that many spikes can still occur independently, without being associated with glitches (e.g., Fig. 1H).

Here, we carry out analysis similar to that presented in Pitfall 1 in order to explore the effect of spikes on ACFs. To identify spikes in the 1051 2-hour segments of vertical component data described in Pitfall 1, we filter the raw data above 1 Hz and correlate with the spike waveform. We then convolve with the acausal spike template as we retain the same processing procedures described in Pitfall 1 and construct a dataset which only comprises spike signals. Identified spikes are manually inspected. On average, each 2-hour record has 15 spikes, compared with 13 glitches. Many of the spikes thus corresponded to glitches as precursors. The LF ACF stacks derived from the spike-only data correlate highly with both ~280s and ~370s phases in DL LF ACF (Fig. 5).

When we repeat the analysis throwing out 10% of windows based on a manual inspection of identified spikes, the phases around ~280s and ~370s become even clearer. These prominent artifacts, close to phases reported by Deng and Levander (2020), result from clustering of spikes in time, and agree with the results of Barkaoui et al. (2021) found that glitches and their associated spikes tend to appear in doublets, separated by 280s and 368s. Unlike spikes (or glitches), we lack a clear physics-based model for donks in order to devise a straightforward procedure to remove them. Moreover, to identify and document a complete list of donks in the data stream, a full span of continuous 100 sps, SP data is required. Because this is restricted by the available download bandwidth of SEIS, an alternate means of making reliable estimations is by utilizing the composite SP channel, Energy Short Term Average SP (ESTASP; Lognonné et al., 2019) under the assumption that each strong amplitude excursion corresponds to a donk (Compaire et al., 2021). Here, we calculate vertical component ESTASP data and identify donks (Fig. 1F and G) by applying a standard STA/LTA with identical parameters to those employed by Compaire et al. (2021).

Figure 6 compares detected donks during the quiet hours of the Sol 184 divided into two records (e.g., morning vs. evening hours). The number of identified donks during the evening is substantially larger than the morning of Sol 184 (Fig. 6). During the noisy periods of the Martian Sol, the detection rate becomes even greater but difficult to verify the fidelity of those signals identified as donks because the background noise level is also significantly higher (Fig. 1F and G). A typical signal duration of donk is ~5s and the median timing between donk signals for Sol 184 appears to be ~80s during the morning and ~60s during the evening (Fig. 6). Note that this median delay can be significantly shorter (~10s) during the evening for some Sols (Compaire et al., 2021). We notice the performance of detecting donks is strongly dependent on the choice of the hyperparameters (filter range and length of STA/LTA windows) used in our processing. Further assessment of methods for detecting donks is warranted.

Because the driving force behind the origin of spikes or donks (and glitches) is the large diurnal temperature variations on Mars, it is important to understand how such periodic behavior affects different mechanical components of the *InSight* lander and seismometer within each cycle which cause nonseismic arrivals in noise correlation functions. Unfortunately, effects on donks cannot be fully explored in this study due to the limitation of available data sampled higher than 20 sps, given the limited downlink bandwidth from *InSight*.

<u>Pitfall 3</u>: Lander modes

In contrast to the transient artifacts such as glitches, donks, and spikes, resonant mechanical modes of the *InSight* lander, continuously excited by the wind, are observed and are the first type of sustained signal we will discuss. The lander modes manifest themselves in the frequency domain as distinct spectral peaks (Fig. 7). By analyzing data recorded by the SP seismometer on deck of the lander (Panning et al., 2020) prior to the deployment of SEIS instrument on the Martian surface, Dahmen et al. (in review) associate a total of five strong spectral peaks up to 10 Hz with resonant shaking of the lander and its components. Though these modes vary in frequency with temperature and wind, the modes are identified as 1.6 Hz, 3.3 Hz, 4.1 Hz, 6.8 Hz, 8.6 Hz (Fig. 7). Of these spectral peaks, the mode at 1.6 Hz in particular is only noticeable during evening / night hours (e.g., 22:00 - 05:00 LMST) when moderate wind exists mostly on the vertical component but becomes imperceptible either when the wind noise is high (e.g., during ~6 hours where the power spectra peak as shown in Fig. 7) or during the quiet hours (between 18:00 and 22:00 LMST) of the Martian sol. The rest of the lander modes at 3.3 Hz, 4.1 Hz, 6.8 Hz, and 8.6 Hz are much stronger throughout the record and show a clear indication of variations in frequency during the noisy period as they become stable after 18:00 LMST (Fig. 7-8). Such strong variations of those spectral peaks are driven by temperature changes induced by wind on Mars (Clinton et al., 2021). There are other "temporary" modes that are intermittently observed at 2.7 Hz, 3.7 Hz, 5.3 Hz and a few more at higher frequencies (> 6Hz) throughout different periods of time in our records (Dahmen et al., in review). Note that while a few strong resonances above 10 Hz are also observed mainly on the SP seismometer, we will not discuss them here because they are above the Nyquist frequency of the acquisition of the SEIS-VBB data sampled at 20 Hz (see Dahmen et al., in review for more detail on lander modes).

We quantitatively assess the effect of the lander modes and their frequency variations on the expected ACFs constructed from SEIS-VBB data. We start with the measurements of lander mode frequency, spectral width and amplitude made by Dahmen et al. (in review) for 7 Sols (185, 225, 345, 425, 505, 585 and 625). Measurements of each quantity are averaged over the 7 Sols, and used to construct the representative power spectrum for each 30 minute window (with 70% overlap) of the Martian day, and are shown in Fig. 8A (alongside the tick signal discussed in the next section). Because of the weak visibility of the 8.6 Hz lander mode, its spectral width is estimated and set to the median width of the 6.8 Hz mode. The ACFs for each 30-minute window are given by the inverse Fourier Transform of these representative power spectra. The ACFs resulting from each solitary lander mode (Fig. 8B) oscillate and decay rapidly with lag-time, having negligible power at lag times greater than 4 s for all but the 3.3 Hz mode, which exhibits energy in the ACF out to 8 s lag time.

Because temperature and wind conditions vary systematically during the course of the Martian day, the lander mode frequencies also show systematic variations; as a result, the oscillations in the ACFs also vary with time of day. When ACFs are stacked, either by simple summation or by more sophisticated means such as phase-weighted stacking, these variations produce a beating effect, and can give rise to coherent "arrivals" (Fig. 8B). These arrivals are particularly prominent when phase-weighted stacking is used. For the 3.3 Hz and 4.1 Hz lander modes, arrivals at ~5s and ~4s are observed, respectively; these could easily be misinterpreted as resulting from structural layering in the subsurface. Variations in frequency of the other lander modes (6.8 Hz and 8.6 Hz) are larger, and the resulting beating effect produces apparent arrivals at smaller lag times.

Suemoto et al. (2020) used 1-minute segmented ambient noise records and computed ACFs for SEIS-VBB data bandpass filtered between 5 - 7 Hz. The authors identified coherent arrivals at 0.6 and 1.1s and interpreted them as lithological reflectors beneath the *InSight* lander. However, the timings of those arrivals coincide with the ACFs derived from one of the strongest lander modes at 6.8 Hz (Fig. 8B). This is also consistent with their polarization analysis of data > 2 Hz that showed a backazimuth dominantly pointing toward the direction of the lander (Suemoto et al., 2020). Hence, the structural interpretation of 0.6s and 1.1s arrivals should be reassessed after eliminating the lander mode at 6.8 Hz.

When all four lander modes are included in a potential autocorrelation analysis, their frequency variations due to temperature changes give rise to a complex ACF when stacked over the course of a Martian day (Fig. 8C). While the precise appearance of the ACFs resulting solely from the lander modes will depend on details such as the precise stacking scheme, relative weighting of signals during various times of day, and even seasonal variations, we find that they have largest signals in the first ~6 s of lag time. Therefore, structural interpretations of the first ~6s of ACFs may be biased by the presence of signals due to lander modes and should be approached with caution.

Pitfall 4: Tick noise

Periodic tick noise is the most consistent idiosyncratic signal recorded on the SEIS-VBB and SEIS-SP instrument (Fig. 7A and 9). This electrical noise is generated due to the acquisition of temperature measurements, and the corresponding harmonics are visible up to 6 Hz during the quiet hours, with the strongest and weakest on the V and U channels, respectively (Fig. 7C). Note, however that these harmonics sometimes are observed beyond 10 Hz. See Zwifel et al. (in review) for a technical explanation of the origin of the tick noise.

We superimpose the 7 Sol averaged spectral width and amplitude of the 1 Hz tick noise onto the lander mode measurements and compute theoretical ACFs following the same manner as described in the previous section. Unsurprisingly, we find that the ACFs and their stacks show a periodic 1s oscillation predominantly observed after ~ 6 s in addition to those arrivals in the first ~6 s of lag time resulting from the combined effects of the four lander modes (Fig. 8C).

An effective treatment of the tick noise has been devised and should be applied to the data preprocessing step prior to autocorrelation. Compaire et al. (2021) estimate tick noise waveforms on the U, V and W channels by stacking many waveforms segmented by nonoverlapping, 1s moving window during the quiet hours (e.g., 18:00 to 20:00, LMST) when the tick noise is the strongest. This approach provides a relatively stable estimate of the tick noise, as can be seen by the consistent tick pattern across 2-year long records (Fig. 9). After subtracting the estimated tick noise from the raw records, the 1 Hz energy and its overtones are effectively removed while retaining the background ambient noise data (Fig. 7B and D). Alternatively, a series of band-rejection or notch filters (with relatively small fractional bandwidth; Schimmel et al., 2021), or a comb filter can similarly remove the tick noise in order to avoid such potential contamination (e.g., Knapmeyer-Endrun et al., 2021).

<u>Pitfall 5</u>: 2.4 Hz resonance

The origin of 2.4 Hz resonance, which is visible on both SP and VBB data, remains debated. The overall bandwidth of this feature is the largest among all the sustained peculiarities discussed in the previous sections (Fig. 1 and 7). The 2.4 Hz resonance is persistent throughout the data, but since its amplitude does not strongly vary, it is most pronounced during the quiet periods. There is no indication of frequency shifts of the resonance due to changes in temperature (Dahmen et al., in review). Though its amplitude appears to slightly vary with temperature, this could result from the strong correlation between temperature and wind speed. All observed marsquakes with a spectrum extending to 2.4 Hz show an excitation at this frequency in excess of the noise amplification (Clinton et al., 2020; Compaire et al., 2021) (Fig. 10), unlike all other lander modes described in Pitfall 4. The spectral shape around the 2.4 Hz resonance typically shows a fine structure comprising several noticeable spectral peaks that are different for each component (also in contrast to all other observed modes) (Fig. 11). This spectral signature can easily percolate into the data processing procedure and ultimately dominate ACFs between 1 and 5 Hz derived from ambient noise or event coda which is presumably produced by marsquakes (Fig. 12A).

Here, we take hourly-summed HF ACFs derived from glitch-removed data, and compute their corresponding normalized spectra to examine the variations associated with fine spectral features of the 2.4 Hz resonance (Fig. 11A). Though small variations exist across individual spectra of hourly stacked ACFs, the overall spectral shape largely remains unchanged and can be approximated by several gaussian peaks whose central frequencies fit our data: 2.15 Hz, 2.22 Hz, 2.25 Hz, 2.31 Hz, 2.34 Hz, 2.38 Hz, 2.405 Hz, 2.43 Hz, 2.475 Hz, and 2.51 Hz (Fig. 11B). While elevated energy associated with the 2.4 Hz resonance may extend up to ~2.8 Hz (see Compaire et al., 2021), peaks above 2.51 Hz are relatively weaker and are not explicitly modeled in our analysis (Fig. 11B). We find two strong spectral peaks that are stationary and ubiquitously observed between 2.30 and 2.45 Hz during the quiet hours but their shapes become substantially subdued when background noise increases as the winds pick up (Fig. 11C-D). These two peaks at 2.35 Hz and 2.38 Hz are also coherently excited by most of the HF, VF, and 2.4 Hz marsquake events (Fig. 11E), which also amplify power across the 2.4 Hz more broadly. Intriguingly, a strong spectral peak appears ~2.33 Hz in the marsquake records, but is not seen in the ambient noise during quiet or noisy hours. Similarly, excitation of a peak near 2.5 Hz seen in marsquake records, may represent a shift to lower frequency of a nearby peak seen in the ambient noise data during quiet hours. The rest of the spectral peaks are relatively stable across different hours of the Martian Sol regardless of the disturbance by the wind noise (Fig. 11C-D). A detailed analysis of similarities and differences between fine structure of the 2.4 Hz resonance as seen in ambient noise and marsquake records is, however, beyond the scope of this work.

While some authors favor including the 2.4 Hz resonance in their structural analysis (e.g., Compaire et al., 2021), using ambient noise signals during quiet hours of the Martian Sol, others opt to exclude it from the analysis. Schimmel et al., (2021) explore the data largely outside the 2.4 Hz resonance, compensating for the reduction of signal by broadening the bandwidth used to obtain the ACFs. A key observation to note here is that the crustal phases seen at ~11.5s and 21.0s (discussed in Pitfall 1) are ubiquitous on all HF ACFs produced with or without energy near the 2.4 Hz resonance (Fig. 12A). Crustal structure inferred from independent analysis based on receiver functions supports the interpretation of the ~11.5s and 21.0s phases in terms of two-way travel times of P waves within crustal layers (Lognonné et al., 2020; Knapmeyer-Endrun et al., 2021). On the other hand, the HF ACFs computed including the 2.4 Hz resonance are characterized by a beating effect arising from the fine structure of the broad 2.4 Hz resonance. Notably, such ACFs can be successfully modeled by summing decaying cosines corresponding to the nine frequencies identified in Figure 11. If we assume each of those peaks, i, can be modeled by a Gaussian centered on angular frequency ω_i of standard deviation σ, each Gaussian contributes to the ACF given by the inverse transform (taking into account the symmetric negative frequency contribution) i.e.,

$$ACF = \sum_{i}^{9} a_i \sqrt{2}\sigma \exp(-0.25\sigma^2 t^2) \cos{(\omega_i t)}$$

where a_i are the peak amplitudes, and t is time. The model explains ~90% of the variance of the ACF data with $\sigma = 0.076$ radians/sec (Fig. 12C). Thus, structural inferences based on phases the SP ACFs besides the ~11.5 and 21.0 s peaks should be informed by considerations regarding the origin of the 2.4 Hz resonance (e.g., Fig. 12B).

Recommendations and conclusions:

This work summarizes idiosyncratic signals observed in the ambient seismic recordings of the VBB seismometer on Mars and illustrates how they can manifest when researchers carry out standard data processing procedures that are commonly applied to data acquired on Earth. We also find that such signals can similarly affect the processing of marsquake waveforms. Therefore, a careful examination is required during each data processing step to avoid making incorrect structural inferences based on potentially compromised data.

Based on the analyses presented here, we recommend the following best practices for avoiding spurious signals and biases in interpretations:

Without using properly deglitched waveforms collected by the *InSight* mission, any result from an ambient noise analysis can be heavily contaminated by glitch artifacts, which will depend on the specifics of glitch duration and systematics in glitch separation time. These artifacts can bias interpretation of ACFs, whether the raw data contains ground vibration measurements due to ambient noise or various types of marsquake events. For example, two strong phases in the LF ACFs interpreted as P-wave reflections from the olivine to wadsleyite phase transition and core-mantle boundary of Mars suggested by Deng and Levander (2020) are substantially affected by the presence of glitches. To obtain high fidelity waveforms with minimized contamination by glitches, we recommend a glitch removal procedure informed by the underlying physical process of how the glitch signal is being generated.

Like glitches, spikes can also generate artifacts in ACFs and ultimately lead to biased structural interpretation. While most spikes can be removed because they can be identified alongside glitches, donks are too unpredictable in their timing and not reproducible enough in their signal shape to be reliably identified and removed. Fortunately, they are predominantly observed beyond the Nyquist frequency of the SEIS-VBB acquired at 20 sps (Lognonné et al., 2019). Hence, one could effectively minimize donks compromising the data by restricting the frequency range of the data below 10 Hz.

For analyzing data above 1 Hz, effects of various lander modes should be fully accounted for,as their stability varies throughout the course of the Martian Sol. Because their frequencies and amplitudes fluctuate due to variations in temperature and wind conditions on Mars, respectively, the lander modes should be identified in both time and frequency domain simultaneously with a proper tracking approach calibrated against temperature and wind measurements. Notably, the frequency range of the SP ACFs produced by Suemoto et al. (2020) contains one of the strongest lander modes at 6.8 Hz. Our analysis shows how observed spectral width and amplitude of the 6.8 Hz mode itself can produce artifacts in ACFs whose lag times are comparable to those interpreted in Suemoto et al. (2020). One should also note that there are other temporary modes that are less frequently observed, and potential seasonal variations on the corresponding frequencies should be further investigated.

The repeating 1 Hz pattern and its overtones due to the tick noise is relatively straightforward to address when processing SEIS data. As we illustrate in Pitfall 4, the most effective approach is to estimate the tick noise waveform during the quiet hours using continuous waveforms (preferably without gaps) then remove it from the raw data. Importantly, because temperature measurements -- and, therefore, tick timing -- are controlled by the digitizer clock not by the local on-board time from the AC master clock, tick noise removal is encouraged to be applied before correcting for digitizer clock drift (Zweifel et al., 2021).

Signals of debated origin, such as the 2.4 Hz resonance, can also affect structural inferences we may extract from data that contains this energy (e.g., Fig. 12B). All of the SP ACFs derived from either ambient noise data during quiet hours of the Martian Sol or marsquake coda waveforms show strong 2.4 Hz resonance (Compaire et al., 2021; Knapmeyer-Endrun et al., 2021). This 2.4 Hz resonance may be related to structural resonance due to a near-subsurface layer (Giardini et al., 2020; Pan et al., 2020; van Driel et al. 2021), mechanical noise related to the lander, or both.

The peculiarities identified in the SEIS data can also be found in seismic data collected on Earth and the Moon. For example, Wilson et al. (2017) documented transient pulses embedded in data from a range of broadband sensors installed at stations of the Global Seismographic Network (GSN) which may have been generated by micro-tilt of the sensors due to thermal instability of the environment. Similar temperature-driven artifacts manifested in data from the *Apollo* seismometers accompanying sudden tilts of the instrument resulting from large temperature variations and insufficient thermal insulation (e.g., Nakamura, 2003). Often, sustained signals associated with strong resonances may hinder robust structural interpretation are also observed in various terrestrial datasets, such as the strumming of head-buoy cable from ocean-bottom seismometers (e.g., Stähler et al. 2018) or coupling and decoupling of poles used to anchor seismometers deployed in Greenland (e.g., see Appendix C in Carmichael, 2013). The considerations in treating transient and sustained signals presented in this work can therefore be useful for ensuring reliable structural inferences in these analogous situations on Earth and the Moon. The pitfalls we discuss in the main text are not an exhaustive list. We have only explored a subset of those transient and sustained signals that are most easily noticeable in SEIS-VBB data stream. For example, additional lander modes are strongly observed beyond 10 Hz and these modes should be fully understood before exploring the waveform data collected at 100 sps as we study structures at finer scale. To obtain more detailed information as well as the guidance for eliminating each kind of idiosyncratic signal in the *InSight* data, we suggest readers make use of the articles referred to in the descriptions of each Pitfall. We advise our readers to be cautious about yet unidentified peculiarities which may still exist in data and be sure to properly address those that are identified as a first step when conducting an analysis in Martian seismology.

Data and Resources:

The *InSight* seismic waveform data are available from the IPGP Datacenter, IRIS-DMC (*InSight* Mars SEIS Data Service, 2019) and NASA PDS (http://psd.nasa.gov/). The data are produced and visualized with Python and Matlab scripts, some of which can be obtained from the GitHub repository: https://github.com/UMD-InSight/InSight-seismic-data-downloader.

Acknowledgement:

We acknowledge NASA, CNES, their partner agencies and Institutions (UKSA, SSO, DLR, JPL, IPGP-CNRS, ETHZ, IC, MPS-MPG) and the flight operations team at JPL, SISMOC, MSDS, IRIS-DMC and PDS for providing SEED SEIS data. We thank thorough and thoughtful reviews from Dr. Adam Ringler and an anonymous reviewer that greatly improved the manuscript. DK and PD thank Salma Barkaoui for insightful discussions on glitch clustering. The MPS-MPG SEIS team acknowledges funding for development of the SEIS leveling system by the DLR German Space Agency. DK, RM, and NS acknowledge NASA grant 80NSSC18K1628 for support. VL acknowledges support from the Packard Foundation. The authors acknowledge both Université Fédérale de Toulouse Midi Pyrénées and the Région Occitanie for funding the PhD grant of NC. MS thanks SANIMS (RTI2018-095594-B-I00). We acknowledge NASA, CNES, their partner agencies and institutions (UKSA, SSO, DLR, JPL, IPGP-CNRS, ETHZ, IC, MPS-MPG). French authors are supported by ANR MAGIS (ANR-19-CE31-0008-08) and by CNES for SEIS science support. This paper is InSight Contribution Number 217.

References:

Anderson, J. F., & Lees, J. M. (2014). Instrument Corrections by Time-Domain Deconvolution.

Seismological Research Letters, *85*(1), 197-201.

Banerdt, W. B., Smrekar, S. E., Banfield, D., Giardini, D., Golombek, M., Johnson, C. L., ... & Wieczorek, M. (2020). Initial results from the InSight mission on Mars. *Nature Geoscience*, *13*(3), 183-189.

Banfield, D., Rodriguez-Manfredi, J. A., Russell, C. T., Rowe, K. M., Leneman, D., Lai, H. R., ... & Banerdt, W. B. (2019). InSight auxiliary payload sensor suite (APSS). *Space Science Reviews*, *215*(1), 1-33.

Banfield, D., Spiga, A., Newman, C., Forget, F., Lemmon, M., Lorenz, R., ... & Banerdt, W. B. (2020). The atmosphere of Mars as observed by InSight. *Nature Geoscience*, *13*(3), 190-198.

Barkaoui, S., Lognonné, P. H., Dehoop, M., Drilleau, M., Kawamura, T., Stutzmann, E., ... & Murdoch, N. (2019, December). Unsupervised representation learning for clustering SEIS data in continuous records with deep scattering network. In *AGU Fall Meeting Abstracts* (Vol. 2019, pp. DI51A-0017).

Bensen, G. D., Ritzwoller, M. H., Barmin, M. P., Levshin, A. L., Lin, F., Moschetti, M. P., ... & Yang, Y. (2007). Processing seismic ambient noise data to obtain reliable broad-band surface wave dispersion measurements. *Geophysical Journal International*, *169*(3), 1239-1260.

Beyreuther, M., Barsch, R., Krischer, L., Megies, T., Behr, Y. and Wassermann, J., 2010. ObsPy: A Python toolbox for seismology. *Seismological Research Letters*, 81(3), pp.530-533.

Boore, D. M., & Bommer, J. J. (2005). Processing of strong-motion accelerograms: needs, options and consequences. *Soil Dynamics and Earthquake Engineering*, *25*(2), 93-115.

Carmichael, J. D. (2013). Melt-triggered seismic response in hydraulically-active polar ice:

Observations and methods. PhD thesis, Univ. of Wash., Seattle, http://hdl.handle.net/1773/25007.

Ceylan, S., Clinton, J. F., Giardini, D., Böse, M., Charalambous, C., van Driel, M., ... & Perrin, C. (2020). Companion guide to the marsquake catalog from InSight, Sols 0–478: Data content and non-seismic events. *Physics of the Earth and Planetary Interiors*, *310*, 106597.

Charalambous, C., Stott, A. E., Pike, W. T., McClean, J. B., Warren, T., Spiga, A., ... & Banerdt, W. B. (2021). A comodulation analysis of atmospheric energy injection into the ground motion at InSight, Mars. *Journal of Geophysical Research: Planets*, e2020JE006538.

Clinton, J., Giardini, D., Böse, M., Ceylan, S., van Driel, M., Euchner, F., ... & Teanby, N. A. (2018). The Marsquake service: Securing daily analysis of SEIS data and building the Martian seismicity catalogue for InSight. *Space Science Reviews*, *214*(8), 1-33.

Clinton, J. F., Ceylan, S., van Driel, M., Giardini, D., Stähler, S. C., Böse, M., ... & Stott, A. E. (2021). The Marsquake catalogue from InSight, sols 0–478. *Physics of the Earth and Planetary Interiors*, *310*, 106595.

Compaire, N., Margerin, L., Garcia, R. F., Pinot, B., Calvet, M., Orhand-Mainsant, G., ... & Banerdt, W. B. (2021). Autocorrelation of the ground vibrations recorded by the SEIS-InSight seismometer on Mars. *Journal of Geophysical Research: Planets*, e2020JE006498.

Dahmen, N. L., Zenhausern, G., Clinton, J. F., Giardini, D., S. Stahler, Ceylan, S., ... & Banerdt, B. W. (2021). Resonances and lander modes observed by InSight on Mars (1-9 Hz), in review

Deen, M., Wielandt, E., Stutzmann, E., Crawford, W., Barruol, G., & Sigloch, K. (2017). First observation of the Earth's permanent free oscillations on ocean bottom seismometers. *Geophysical Research Letters*, *44*(21), 10-988.

Deng, S., & Levander, A. (2020). Autocorrelation reflectivity of Mars. *Geophysical Research Letters*, *47*(16), e2020GL089630.

van Driel, M., Ceylan, S., Clinton, J. F., Giardini, D., Horleston, A., Margerin, L., ... & Banerdt, W. B. (2021). High-Frequency Seismic Events on Mars Observed by InSight. *Journal of Geophysical Research: Planets*, *126*(2), e2020JE006670.

Dybing, S. N., Ringler, A. T., Wilson, D. C. & Anthony, R. E. (2019). Characteristics and Spatial Variability of Wind Noise on Near-Surface Broadband Seismometers. Bulletin of the Seismological Society of America. 109 (3): 1082-1098. DOI: http://doi.org/10.1785/0120180227

Folkner, W. M., Dehant, V., Le Maistre, S., Yseboodt, M., Rivoldini, A., Van Hoolst, T., ... & Golombek, M. P. (2018). The rotation and interior structure experiment on the InSight mission to Mars. *Space Science Reviews*, *214*(5), 1-16.

Forbriger, T. Reducing magnetic field induced noise in broad-band seismic recordings. *Geophys. J. Int.* (2007) 169, 240–258 doi: 10.1111/j.1365-246X.2006.03295.x

Gorbatov, A., Saygin, E., & Kennett, B. L. N. (2013). Crustal properties from seismic station autocorrelograms. Geophysical Journal International, 192(2), 861-870.

Giardini, D., Lognonné, P., Banerdt, W. B., Pike, W. T., Christensen, U., Ceylan, S., ... & Yana, C. (2020). The seismicity of Mars. *Nature Geoscience*, *13*(3), 205-212.

InSight Mars SEIS Data Service. (2019). SEIS raw data, InSight Mission. IPGP, JPL, CNES, ETHZ, ICL, MPS, ISAE-Supaero, LPG, MFSC. https://doi.org/10.18715/SEIS.INSIGHT.XB_2016

InSight Marsquake Service. (2021). Mars Seismic Catalogue, InSight Mission; V6 2021-04-01 (Version 6.0) [Data set]. ETHZ, IPGP, JPL, ICL, MPS, Univ. Bristol. https://doi.org/10.12686/A11

Ito, Y., & Shiomi, K. (2012). Seismic scatterers within subducting slab revealed from ambient noise autocorrelation. Geophysical research letters, 39(19).

Kanamori, H., & Rivera, L. (2008). Source inversion ofWphase: speeding up seismic tsunami warning. Geophysical Journal International, 175(1), 222-238.

Kim, D., Keranen, K. M., Abers, G. A., & Brown, L. D. (2019a). Enhanced resolution of the subducting plate interface in Central Alaska from autocorrelation of local earthquake coda. Journal of Geophysical Research: Solid Earth, 124(2), 1583-1600.

Khan, A., S. Ceylan, M. van Driel, D. Giardini, P. Lognonné, H. Samuel, N. C. Schmerr, S. C. Stähler, A.C. Duran, Q. Huang, D. Kim, ... & W. B. Banerdt. Imaging the upper mantle structure of Mars with InSight seismic data, *Science,* 373, 434-438.

Kim, D., & Lekic, V. (2019b). Groundwater variations from autocorrelation and receiver functions. *Geophysical Research Letters*, *46*(23), 13722-13729.

Knapmeyer-Endrunm B., Panning, M., Bissig, F., Joshi, R., Khan, A., Kim, D., … & Banerdt, B. W. (2021), Thickness and structure of the Martian crust from InSight seismic data *Science*, 373, 438-443.

Latham, G., Ewing, M., & Sutton, G. (1969). The Apollo passive seismic experiment. *Science*, *165*(3890), 241-250.

Lecocq, T., Hicks, S. P., Van Noten, K., Van Wijk, K., Koelemeijer, P., De Plaen, R. S., ... & Xiao, H. (2020). Global quieting of high-frequency seismic noise due to COVID-19 pandemic lockdown measures. *Science*, *369*(6509), 1338-1343.

Lin, F. C., Tsai, V. C., Schmandt, B., Duputel, Z., & Zhan, Z. (2013). Extracting seismic core phases with array interferometry. *Geophysical Research Letters*, *40*(6), 1049-1053.

Lognonné, P., Banerdt, W. B., Giardini, D., Pike, W. T., Christensen, U., Laudet, P., ... & Mance, D. (2019). SEIS: Insight's seismic experiment for internal structure of Mars. *Space Science Reviews*, *215*(1).

Lognonné, P., Banerdt, W. B., Pike, W. T., Giardini, D., Christensen, U., Garcia, R. F., ... & Zweifel, P. (2020). Constraints on the shallow elastic and anelastic structure of Mars from InSight seismic data. *Nature Geoscience*, *13*(3), 213-220.

Longuet-Higgins, M. S. (1950). A theory of the origin of microseisms. Philosophical Transactions of the Royal Society of London. Series A, *Mathematical and Physical Sciences*, 243(857), 1-35.

Martynov, V. G., Astiz, L., Kilb, D. & Vernon, F. L. (2020). The M2 Tidal Tilt Results from USArray Seismic Data from the Western United States. Bulletin of the Seismological Society of America, 110 (6): 3196–3210. https://doi.org/10.1785/0120190314

Murdoch, N., Alazard, D., Knapmeyer-Endrun, B., Teanby, N. A., & Myhill, R. (2018). Flexible mode modelling of the InSight lander and consequences for the SEIS instrument. *Space Science Reviews*, 214(8), 1-24.

Nakamura, Y. (2003). New identification of deep moonquakes in the Apollo lunar seismic data. *Physics of the Earth and Planetary Interiors*, 139(3-4), 197-205.

Pan, Lu, et al. "Crust stratigraphy and heterogeneities of the first kilometers at the dichotomy boundary in western Elysium Planitia and implications for InSight lander." Icarus 338 (2020): 113511.

Panning, M. P., Pike, W. T., Lognonné, P., Banerdt, W. B., Murdoch, N., Banfield, D., ... &

Warren, T. (2020). On-Deck Seismology: Lessons from InSight for Future Planetary Seismology. *Journal of Geophysical Research: Planets*, *125*(4), e2019JE006353.

Pham, T-S. & Tkalčić H. (2017). On the feasibility and use of teleseismic P wave coda autocorrelation for mapping shallow seismic discontinuities. Journal of Geophysical Research: Solid Earth, 122(5), 3776-3791.

Quiros, D. A., Brown, L. D., & Kim, D. (2016). Seismic interferometry of railroad induced ground motions: Body and surface wave imaging. *Geophysical Supplements to the Monthly Notices of the Royal Astronomical Society*, *205*(1), 301-313.

Retailleau, L., Boué, P., Li, L., & Campillo, M. (2020). Ambient seismic noise imaging of the lowermost mantle beneath the North Atlantic Ocean. *Geophysical Journal International*, *222*(2), 1339-1351.

Romero, P., Schimmel, M., Mapping the basement of the Ebro Basin in Spain with seismic ambient noise autocorrelations, Journal of Geophysical Research, 123, 5052-5067, doi: 10.1029/2018JB015498, 2018.

Sabra, K. G., Gerstoft, P., Roux, P., Kuperman, W. A., & Fehler, M. C. (2005). Extracting time-domain Green's function estimates from ambient seismic noise. *Geophysical Research Letters*, *32*(3).

Schimmel, M., & Paulssen, H. (1997). Noise reduction and detection of weak, coherent signals through phase-weighted stacks. *Geophysical Journal International*, *130*(2), 497-505.

Shapiro, N. M., Campillo, M., Stehly, L., & Ritzwoller, M. H. (2005). High-resolution surface-wave tomography from ambient seismic noise. *Science*, *307*(5715), 1615-1618.

Schimmel, M., Stutzmann, E., Lognonné, P., Compaire, N., Davis, P., Drilleau, M., ... &

Banerdt, B. (2021). Seismic Noise Autocorrelations on Mars. *Earth and Space Science*, e2021EA001755.

Scholz, J. R., Widmer-Schnidrig, R., Davis, P., Lognonné, P., Pinot, B., Garcia, R. F., ... & Banerdt, W. B. (2020). Detection, analysis, and removal of glitches from InSight's seismic data from Mars. *Earth and Space Science*, *7*(11), e2020EA001317.

Snieder, R. (2004). Extracting the Green's function from the correlation of coda waves: A derivation based on stationary phase. *Physical Review E*, *69*(4), 046610.

Spohn, T., Grott, M., Smrekar, S. E., Knollenberg, J., Hudson, T. L., Krause, C., ... & Banerdt, W. B. (2018). The heat flow and physical properties package (HP 3) for the InSight mission. *Space Science Reviews*, *214*(5), 1-33.

Stähler, S. C., Sigloch, K., Hosseini, K., Crawford, W. C., Barruol, G., Schmidt-Aursch, M. C., ... & Deen, M. (2016). Performance report of the RHUM-RUM ocean bottom seismometer network around La Réunion, western Indian Ocean. *Advances in Geosciences*, *41*, 43-63.

Stähler, S.C., Schmidt-Aursch, M.C., Hein, G., Mars, R., 2018. A Self-Noise Model for the German DEPAS OBS Pool. *Seismological Research Letters* 89, 1838–1845.

Stähler S. C., Khan, A., Bruce, B., Lognonné, P., Giardini, D., Ceylan S., Drilleau, M., Duran, A. C., Garcia, R., Huang, Q., Kim, D., … & Smrekar, S. E. (2021), Seismic detection of the Martian Core, *Science*, 373, 443-448.

Stutzmann, E., Schimmel, M., Lognonné, P., Horleston, A., Ceylan, S., van Driel, M., ... & Spiga, A. (2021). The polarization of ambient noise on Mars. *Journal of Geophysical Research: Planets*, *126*(1), e2020JE006545.

Suemoto, Y., Ikeda, T., & Tsuji, T. (2020). Temporal variation and frequency dependence of seismic ambient noise on Mars from polarization analysis. *Geophysical Research Letters*, *47*(13), e2020GL087123.

Sutton, G.H., Duennebier, F.K., Iwatake, B., 1981. Coupling of ocean bottom seismometers to soft bottom. *Marine Geophysical Researches* 5, 35–51.

Tape, C., Ringler, A. T., & Hampton, D. L. (2020). Recording the aurora at seismometers across Alaska. *Seismological Society of America*, *91*(6), 3039-3053.

Trehu, A.M., 1985. A note on the effect of bottom currents on an ocean bottom seismometer. *Bulletin of the Seismological Society of America* 75, 1195–1204.

Webb, S. C. (2007). The Earth's 'hum'is driven by ocean waves over the continental shelves. *Nature*, 445(7129), 754-756.

Wielandt, E. (2012) Seismic sensors and their calibration. - In: Bormann, P. (Ed.), New Manual of Seismological Observatory Practice 2 (NMSOP-2), Potsdam : Deutsches GeoForschungsZentrum GFZ, 1-51. https://doi.org/10.2312/GFZ.NMSOP-2_ch5

Wielandt, E., & Streckeisen, G. (1982). The leaf-spring seismometer: Design and performance. *Bulletin of the Seismological Society of America*, *72*(6A), 2349-2367.

Zweifel, P., Mance, D., ten Pierick, J., Giardini, D., Schmelzbach, C., Haag, T., Nicollier, T., … & Banerdt, W. B. (2021). Seismic High-resolution acquisition electronics for the NASA InSight mission on Mars, in review.

Authors' postal mailing addresses

Doyeon Kim
University of Maryland
Department of Geology

8000 Regents Dr.
College Park, MD, 20742
United States of America

Paul Davis
University of California
Department of Earth, Planetary and Space Sciences
595 Charles Young Drive East,
Los Angeles, CA, 90095-1567
United States of America

Ved Lekić
University of Maryland
Department of Geology
8000 Regents Dr.
College Park, MD, 20742
United States of America

Ross Maguire
University of Maryland
Department of Geology
8000 Regents Dr.
College Park, MD, 20742
United States of America

Nicolas Compaire
Institut Supérieur
de l'Aéronautique et de l'Espace

10, avenue Edouard-Belin
BP 54032-31055 Toulouse CEDEX 4
France

Martin Schimmel
Geosciences Barcelona – CSIC,
c/ Lluis Sole i Sabaris, s/n
08028 Barcelona
Spain

Elenore Stutzmann
Planétologie et Sciences Spatiales
Université de Paris
Institut de Physique du Globe de Paris
35, rue Hélène Brion
75013 Paris
France

Jessica C. E. Irving
School of Earth Sciences
University of Bristol
Queens Road
Bristol, BS8 1QU
UK

Philippe Lognonné
Planétologie et Sciences Spatiales
Université de Paris

Institut de Physique du Globe de Paris
35, rue Hélène Brion
75013 Paris
France

John-Robert Scholz
Max Planck Institute for Solar System Research
Justus-von-Liebig-Weg 3
37077 Göttingen
Germany

John Clinton
Swiss Seismological Service
ETH Zürich
Sonneggstrasse 5
8092 Zürich
Switzerland

Géraldine Zenhäusern
Department of Earth Sciences
ETH Zürich
Sonneggstrasse 5
8092 Zürich
Switzerland

Nikolaj Dahmen
Department of Earth Sciences
ETH Zürich

Sonneggstrasse 5
8092 Zürich
Switzerland

Sizhuang Deng
Earth, Environmental and Planetary Sciences
Rice University
6100 Main Street
Houston, TX 77005
United States of America

Alan Levander
Earth, Environmental and Planetary Sciences
Rice University
6100 Main Street
Houston, TX 77005
United States of America

Mark Panning
Jet Propulsion Laboratory
California Institute of Technology
4800 Oak Grove Drive
M/S 183-301
Pasadena, CA 91109
United States of America

Raphaël F. Garcia
Institut Supérieur

de l'Aéronautique et de l'Espace
10, avenue Edouard-Belin
BP 54032-31055 Toulouse CEDEX 4
France

Domenico Giardini
Department of Earth Sciences
ETH Zürich
Sonneggstrasse 5
8092 Zürich
Switzerland

Ken Hurst
Jet Propulsion Laboratory
California Institute of Technology
4800 Oak Grove Drive
Pasadena, CA 91109
United States of America

Brigitte Knapmeyer-Endrun
Bensberg Observatory
University of Cologne
Vinzenz-Pallotti-Str. 26
D-51429 Bergisch Gladbach
Germany

Francis Nimmo
Department of Earth and Planetary Sciences

University of California Santa Cruz
Santa Cruz, CA 95064
United States of America

Tom Pike
Department of Electrical and Electronic Engineering
Imperial College London
South Kensington Campus
London SW7 2AZ
UK

Laurent Pou
Department of Earth and Planetary Sciences
University of California Santa Cruz
Santa Cruz, CA 95064

Nicholas Schmerr
University of Maryland
Department of Geology
8000 Regents Dr.
College Park, MD, 20742
United States of America

Simon C. Stähler
Department of Earth Sciences
ETH Zürich
Sonneggstrasse 5
8092 Zürich

Switzerland

Benoit Tauzin
Laboratoire de Géologie de Lyon : Terre, Planètes, Environnement
Université de Lyon
69622 Villeurbanne Cedex
France

Rudolf Widmer-Schnidrig
Black Forest Observatory
Institute of Geodesy
University of Stuttgart
77709 Wolfach
Germany

William B. Banerdt
Jet Propulsion Laboratory
California Institute of Technology
4800 Oak Grove Drive
M/S 321-B60
Pasadena, CA 91109
United States of America

List of figure captions

Figure 1. Seismic ambient noise recordings at Mars. (A) Raw unfiltered ground vibration measurements on U, V, and W channels of SEIS-VBB during Sol 184 (2019-06-03UTC 06:00 –

2019-06-04UTC 08:00), (B) the timings of identified glitches on each channel, and (C) the spectrogram of the U component record, showing a clear change in power spectra density (PSD) due to diurnal wind noise at Mars (between 18:00 and 22:00 Local Mean Solar Time, LMST). Notably, various nonseismic energy manifests in the data along with the real ground shaking measured on the surface of Mars. See main text for details and characteristics on those idiosyncratic signals. (D) Vertical component waveform in acceleration and (E) its corresponding spectrogram after rotating the raw UVW channels and removing the instrument response. (F) A composite SP channel (computed on the spacecraft and continuously transmitted) Energy Short Term Average SP (ESTASP) vertical component data and (G) the timings of identified donks. This ESTASP serves as a reliable estimate for quality assurance of the SP data since retrieving a full span of continuous SP data is restricted by the data acquisition of SEIS. See Pitfall 2 for more details on ESTASP. Inset shows an example of donk waveforms from SP data. (H) Waveform samples of a typical glitch. Glitches in data are often preceded by a high-frequency precursor (or the spike). (I) time-averaged tick noise recorded on U, V, and W channels. . Here, waveforms of the tick noise are estimated by segmenting the raw data during quiet hours of the Martian Sol into non-overlapping, 1s records, then average for each component. (J) Power spectral density (PSD) of our data in (A). Energy associated with the tick noise and its overtones as well as other lander modes are apparent across different spectral peaks (see more details in Fig. 7C).

Figure 2. Distribution of identified glitches on the vertical component of SEIS-VBB data. (A) Distribution of identified glitches by template matching on the vertical component of SEIS-VBB data (the first approach described in main text) recorded during February - July, 2019. Ambient noise waveform data is segmented into a total of 1051, 2-hour records. (B) The comparison of 2-

hour long raw vertical component data vs. glitch-only data recorded during quiet and noisy periods of the Martian Sol. Waveforms plotted correspond to the records marked by orange lines in (A). (C) A typical raw glitch waveform in counts, and (D) pseudo physical units after naive (i.e., zero-phase as opposed to a procedure which preserves causality) instrument response removal. Here, output waveforms are normalized to its peak amplitude. Note that application of the commonly-used instrument response removal built-in within the Obspy Python module, generates nonphysical waveform shapes. See more details in Pitfall 1. (E) A properly deconvolved glitch waveform should appear as a step function in acceleration, as it does upon instrument response removal following Kanamori and Rivera, (2008) (green) and Anderson and Lees (2014) (black), to estimate the response of the VBB system (e.g., Wielandt and Streckeisen, 1982).

Figure 3. Autocorrelation functions (ACFs) of glitch-only waveforms. (A) Individual ACFs computed based on 2-hour long records that only contain identified glitches (e.g., orange, Fig. 2B). Both HF and LF ACFs are considered in two frequency ranges of 0.625 - 2.5 (left panels) Hz and 0.05 - 0.1 Hz (right panels), respectively. Black traces are ACF stacks by a phase weighted stacking. White vertical lines indicate the timing of interpreted phases in Deng and Levander (2020). (B) Same as (A) but using a different vertical component dataset (March - September, 2019) of the 2-hour long records only containing identified glitches following Scholz et al. (2020). (C) Normalized amplitude spectra of the ACF stacks in (A-B). The inset shows a typical shape of the acausal glitch (e.g., Fig. 2D) found in each dataset. *Note this glitch signal in velocity is nonphysical and has a distinctive shape due to an implementation of acausal filtering during instrument removal. The difference in frequency of the larger spectral peaks (i.e., 0.0167 Hz) gives rise to coherent arrivals that can be observed on both HF and LF ACFs, and corresponds to the

apparent duration of the dominant glitch signal (i.e. 60s) . Timings of coherent ACF arrivals also depend on the shape of sidelobes and input parameters for a prefilter (e.g., orange, inset). Because not all acausal glitch signals have identical signal duration, multiple arrivals in ACFs can simultaneously be generated.

Figure 4. Comparison of the ACF stacks with different datasets obtained in our analysis. (A) Phase weighted stacks of HF and (B) LF ACFs based on 2-hour long raw vertical component data between February and July, 2019 (blue, Dataset 2), data with glitches identified and removed (black, Dataset 3), and data with only identified glitch signals (orange, Dataset 1). Each set of ACFs are computed following the data processing procedure in Deng and Levander (2020), so ACF stacks in blue are replicas of the ACFs shown in Deng and Levander (2020). The ACF stacks in green are similarly obtained using a different set of 2-hour long records between March and September, 2019 where glitches are removed by the procedure followed by Scholz et al. (2020). (C) Comparison of the phase weighted stacks of HF and (D) LF ACFs using the Dataset 1 omitting various normalization steps employed by Deng and Levander (2020): temporal balancing (b1), spectral whitening (b2), and both (b3). NB: Abbreviation on each trace in (C-D) denotes, TB = temporal balancing and SW = spectral whitening.

Figure 5. Effect of spikes in the ACF stacks.

Phase weighted stacks of LF ACFs based on 2-hour long vertical component data between February and July, 2019 (blue) compared to those computed using only signals of detected spikes (orange). Each set of ACFs is computed following the data processing procedure in Deng and Levander (2020). Spikes were detected in 1049 out of 1051 traces, and manually inspected to discard outliers, yielding spike-only ACFs with 1001 and 963 traces. Correlation coefficients between our spike-only LF ACF and DL LF ACF are computed around ~280s and ~375s phases (in shaded region) and shown on the right.

Figure 6. ESTASP amplitudes and distribution of the identified donks during quiet hours of Sol 184. ESTASP amplitudes and the timings associated with identified donks during the quiet hours of Sol 184, exclusively processed with data shown in Fig. 1F from (A) the first 16200s and (B) from 66000s to the end of the record. Donk signals are identified with a standard algorithm of STA/LTA a window length of 1s and 25s on each ESTASP channel. Data outside these time ranges are extremely noisy due to strong diurnal wind stresses hence it is difficult to verify the fidelity of identified donks and it requires a full span of complete SP data.

Figure 7. Comparison of the spectrograms of the ambient noise recording with and without the tick noise removal. (A) Spectrograms of the raw ambient noise data recorded on U, V, and W components during one day of Sol 184. White dashed box indicates observed tick noise at 1 Hz. (B) Same as (A) but after applying a tick noise removal procedure. For each channel, the tick noise waveform is estimated exclusively taking data recorded during the quiet hours (e.g., Fig. 1I) then subtracted from raw data following Compaire et al. (2021). (C) Comparison of the PSD for U, V, and W components during noisy vs. quiet hours. The tick noise at 1 Hz is strongly observed for both noisy and quiet hours. Notice during quiet hours however the corresponding harmonics are visible up to 6 Hz in the Sol 184 record. Given our understanding of the root cause of the tick noise we expect that these harmonics also exist above 10Hz. (D) Same as (C) but after applying a tick noise removal procedure described in Pitfall 4.

Figure 8. Identified lander modes and their effects on the ACFs. (A) Representative power spectra of the strongest lander modes (e.g., 3.3 Hz, 4.1 Hz, 6.8 Hz, and 8.6 Hz) including the tick noise at 1 Hz for the Martian Sol. Measurements of those lander mode frequencies, spectral widths and amplitudes are averaged for 7 Sols (185, 225, 345, 425, 505, 585, and 625) taking 70% overlapping 30-minute windows. Below, five panels show theoretical ACFs derived from summing the inverse Fourier transform of the representative power spectra for the tick noise and each solitary lander mode. (B) ACFs stacks for each lander mode shown in (A). Dashed black and solid blue traces indicate the mean and phase-weighted ACFs, respectively. (C) Same as (A-B) but incorporating all lander mode frequencies with and without the 1 Hz tick noise.

Figure 9. Overview of tick noise throughout the *InSight* seismic data. Tick noise, as obtained by stacking for each Sol the raw 20 sps data from 18:00 to 22:00 LMST on a 3s repeating window for (A) VBB-BHU and (B) SP1 records, yields the tick pattern repeating three times. Loss of the pattern between Sols 500 and 750 is due to the large amplitude ambient noise recorded during this period. Apart from that, the tick pattern is very consistent. Because the tick noise has an electromagnetic coupling origin, its amplitude in digital units is roughly proportional to the gain of the sensor feedback, which is much larger on the VBB than on the SP (Lognonné et al., 2019).

Figure 10. High frequency Marsquake waveforms and their corresponding normalized spectra. (A) Average three-component envelopes aligned on P-arrival (t = 0s) from a total of 70 marsquakes from the high frequency family that include high frequency (HF), very high frequency (VF), and the 2.4 Hz events, and the corresponding (B) vertical component waveforms. All MQS

events with the event quality C or above are selected between Sol 128 and 500 (InSight Marsquake Service, 2021) but those with noticeable glitches in the analysis window are removed. For each event, we use a standard algorithm of STA/LTA triggering on the Hilbert envelope averaged across components to pick the Pg- and Sg-arrivals. Both envelopes and waveforms are sorted by the travel time between Sg and Pg picks. See van Driel et al. (2021) for more detailed analysis on these events. (C) Normalized amplitude spectra for each individual event averaged across three-components and (D) the event sum based on different high frequency event types.

Figure 11. Hourly stacked ACFs and the 2.4 Hz resonance. (A) Normalized spectra of hourly summed SP ACFs using our glitch-removed records between February - July, 2019 (Dataset 2) and the corresponding (B) modeled spectra estimated by ten gaussian pulses whose central frequencies fit our data: 2.15 Hz, 2.22 Hz, 2.25 Hz, 2.31 Hz, 2.34 Hz, 2.38 Hz, 2.405 Hz, 2.43 Hz, 2.475 Hz, and 2.51 Hz. (C) Comparison of observed (line with a single color) vs. estimated mean spectra (line with the same color scheme used for (A-B)) of HF ACFs during noisy and (D) quiet hours during the Martian Sol. Gray lines indicate individual hourly spectra models in (B). (E) Observed mean spectra of HF ACFs (C-D) and the three-component average event sum in Fig. 10D.

Figure 12. Comparison of the HF ACF stacks in the literature and structural implications. (A) The HF ACF stacks produced by various author groups in the literature. The first 5s of data is removed due to various source effects. For each ACF, the five Pitfalls discussed in the main text are either removed or treated differently prior to autocorrelation. NB: Labels used as table headers denote, G = Glitches; S & D = Spikes and Donks; Tick = Tick noise; LMs = Lander modes; 2.4

Hz = the 2.4 Hz resonance. Labels used for HF ACFs denote, *DL = the replicated HF ACF stack followed by Deng and Levander (2020) bandpass filtered between 1- 3 Hz; NC1 = ambient noise HF ACF stack and NC2 = HF event family coda ACF stack in Compaire et al. (2021); BK1 = ambient noise HF ACF stack and BK2 = HF event coda ACF stack in Knapmeyer-Endrun et al. (2021) (see traces labeled as C3 and C1 in Fig. 3); MS = HF ACF stack in Schimmel et al. (2021). (B) Two main working hypotheses on the origin of the 2.4 Hz resonance visible in the ACFs: resonance generated by a subsurface structure of Mars and/or another unexplained mode related to the lander. (C) Modeled ACF synthesized by summing nine decaying cosine functions whose frequencies correspond to the spectral peaks observed in the 2.4 Hz resonance in Fig. 10 decaying with a single attenuation parameter. ACF data (red) behind the synthetic ACF is the same plotted as blue trace in (A).

Figures

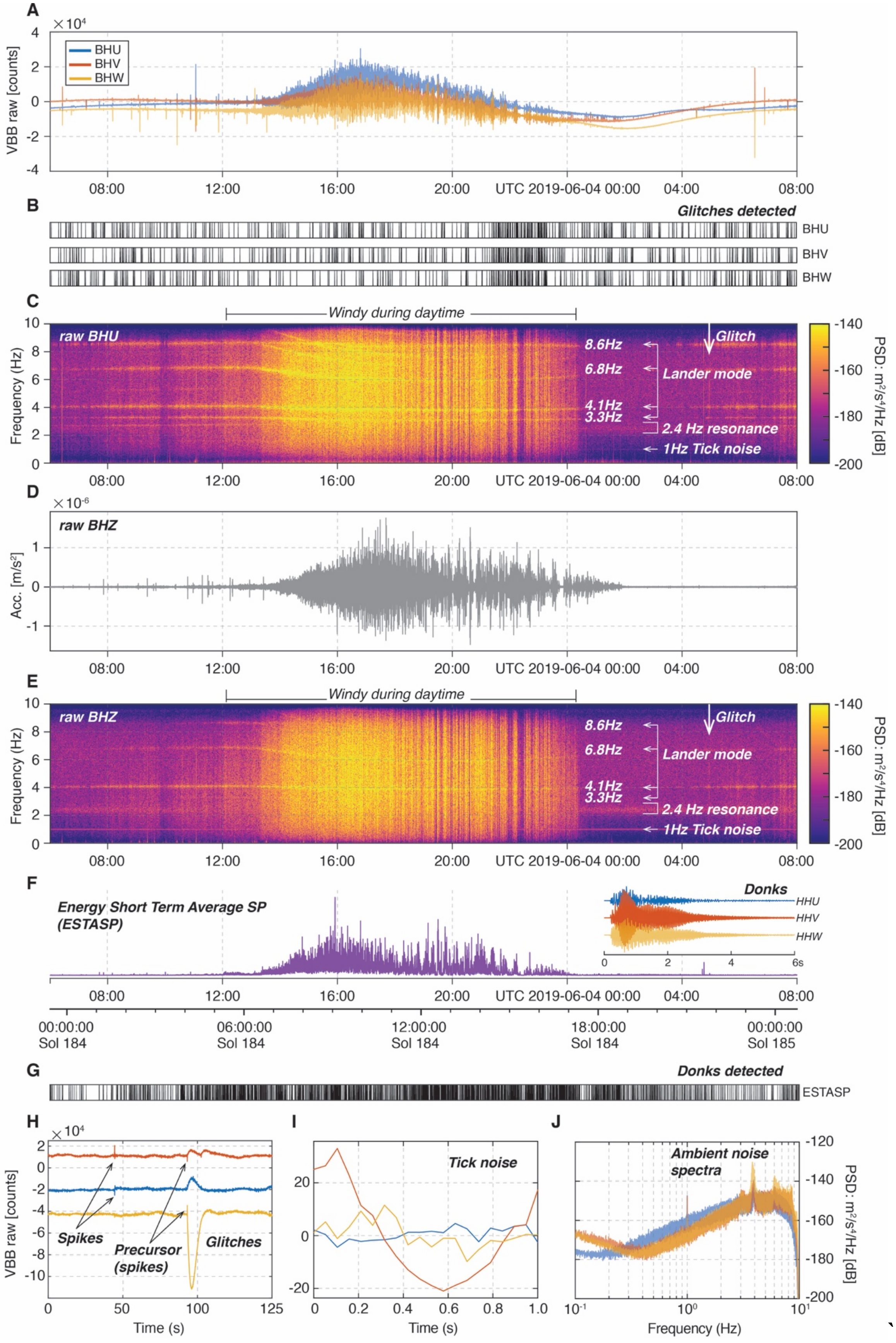
A
×10⁴
BHU
BHV
BHW
VBB raw [counts]
4
2
0
-2
-4
08:00
12:00
16:00
20:00
UTC 2019-06-04 00:00
04:00
08:00
B
Glitches detected
BHU
BHV
BHW
C
Windy during daytime
raw BHU
Glitch
8.6Hz
6.8Hz
Lander mode
4.1Hz
3.3Hz
2.4 Hz resonance
1Hz Tick noise
Frequency (Hz)
PSD: m²/s⁴/Hz [dB]
-140
-160
-180
-200
D
×10⁻⁶
raw BHZ
Acc. [m/s²]
E
Windy during daytime
raw BHZ
F
Energy Short Term Average SP (ESTASP)
Donks
HHU
HHV
HHW
0
2
4
6s
00:00:00 Sol 184
06:00:00 Sol 184
12:00:00 Sol 184
18:00:00 Sol 184
00:00:00 Sol 185
G
Donks detected
ESTASP
H
×10⁴
Spikes
Precursor (spikes)
Glitches
VBB raw [counts]
Time (s)
I
Tick noise
Time (s)
J
Ambient noise spectra
Frequency (Hz)
PSD: m²/s⁴/Hz [dB]
10⁻¹
10⁰
10¹
-120
-140
-160
-180
-200

Figure 1. Seismic ambient noise recordings at Mars. (A) Raw unfiltered ground vibration measurements on U, V, and W channels of SEIS-VBB during Sol 184 (2019-06-03UTC 06:00 – 2019-06-04UTC 08:00), (B) the timings of identified glitches on each channel, and (C) the spectrogram of the U component record, showing a clear change in power spectra density (PSD) due to diurnal wind noise at Mars (between 18:00 and 22:00 Local Mean Solar Time, LMST). Notably, various nonseismic energy manifests in the data along with the real ground shaking measured on the surface of Mars. See main text for details and characteristics on those idiosyncratic signals. (D) Vertical component waveform in acceleration and (E) its corresponding spectrogram after rotating the raw UVW channels and removing the instrument response. (F) A composite SP channel (computed on the spacecraft and continuously transmitted) Energy Short Term Average SP (ESTASP) vertical component data and (G) the timings of identified donks. This ESTASP serves as a reliable estimate for quality assurance of the SP data since retrieving a full span of continuous SP data is restricted by the data acquisition of SEIS. See Pitfall 2 for more details on ESTASP. Inset shows an example of donk waveforms from SP data. (H) Waveform samples of a typical glitch. Glitches in data are often preceded by a high-frequency precursor (or the spike). (I) time-averaged tick noise recorded on U, V, and W channels. . Here, waveforms of the tick noise are estimated by segmenting the raw data during quiet hours of the Martian Sol into non-overlapping, 1s records, then average for each component. (J) Power spectral density (PSD) of our data in (A). Energy associated with the tick noise and its overtones as well as other lander modes are apparent across different spectral peaks (see more details in Fig. 7C).

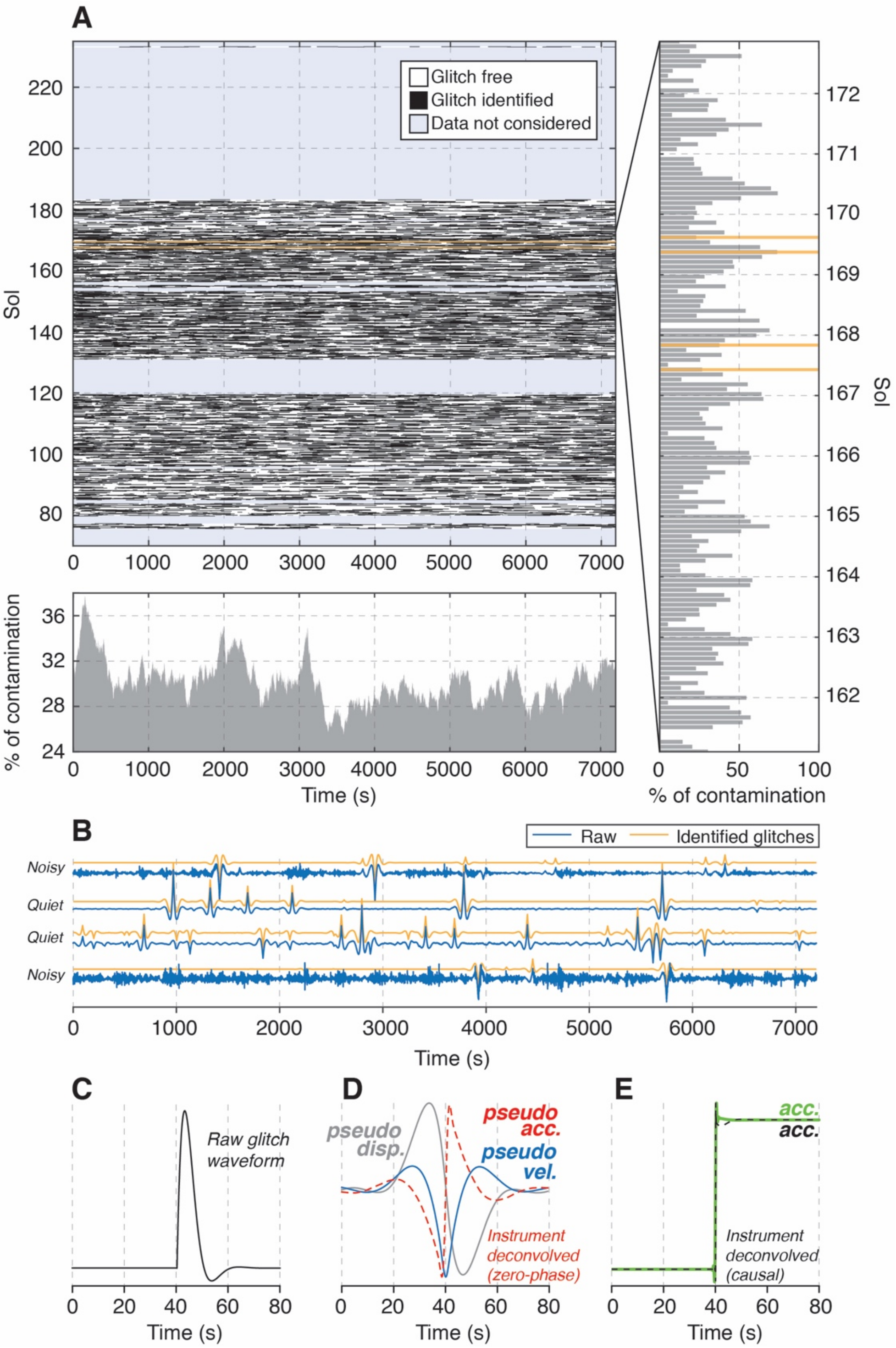

Figure 2. Distribution of identified glitches on the vertical component of SEIS-VBB data. (A) Distribution of identified glitches by template matching on the vertical component of SEIS-VBB data (the first approach described in main text) recorded during February - July, 2019. Ambient noise waveform data is segmented into a total of 1051, 2-hour records. (B) The comparison of 2-hour long raw vertical component data vs. glitch-only data recorded during

quiet and noisy periods of the Martian Sol. Waveforms plotted correspond to the records marked by orange lines in (A). (C) A typical raw glitch waveform in counts, and (D) pseudo physical units after naive (i.e., zero-phase as opposed to a procedure which preserves causality) instrument response removal. Here, output waveforms are normalized to its peak amplitude. Note that application of the commonly-used instrument response removal built-in within the Obspy Python module, generates nonphysical waveform shapes. See more details in Pitfall 1. (E) A properly deconvolved glitch waveform should appear as a step function in acceleration, as it does upon instrument response removal following Kanamori and Rivera, (2008) (green) and Anderson and Lees (2014) (black), to estimate the response of the VBB system (e.g., Wielandt and Streckeisen, 1982).

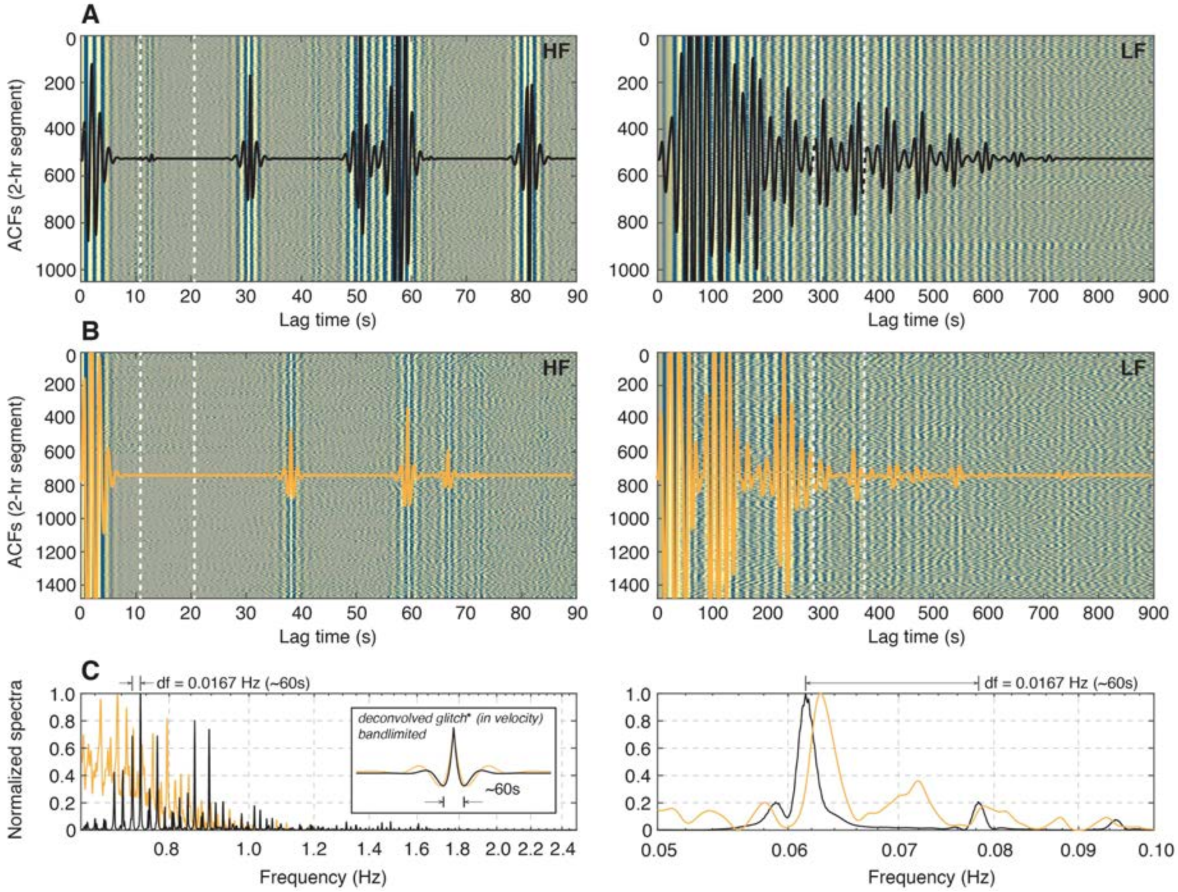

Figure 3. Autocorrelation functions (ACFs) of glitch-only waveforms. (A) Individual ACFs computed based on 2-hour long records that only contain identified glitches (e.g., orange, Fig. 2B). Both HF and LF ACFs are considered in two frequency ranges of 0.625 - 2.5 (left panels) Hz and 0.05 - 0.1 Hz (right panels), respectively. Black traces are ACF stacks by a phase weighted stacking. White vertical lines indicate the timing of interpreted phases in Deng and

Levander (2020). (B) Same as (A) but using a different vertical component dataset (March - September, 2019) of the 2-hour long records only containing identified glitches following Scholz et al. (2020). (C) Normalized amplitude spectra of the ACF stacks in (A-B). The inset shows a typical shape of the acausal glitch (e.g., Fig. 2D) found in each dataset. *Note this glitch signal in velocity is nonphysical and has a distinctive shape due to an implementation of acausal filtering during instrument removal. The difference in frequency of the larger spectral peaks (i.e., 0.0167 Hz) gives rise to coherent arrivals that can be observed on both HF and LF ACFs, and corresponds to the apparent duration of the dominant glitch signal (i.e. 60s) . Timings of coherent ACF arrivals also depend on the shape of sidelobes and input parameters for a prefilter (e.g., orange, inset). Because not all acausal glitch signals have identical signal duration, multiple arrivals in ACFs can simultaneously be generated.

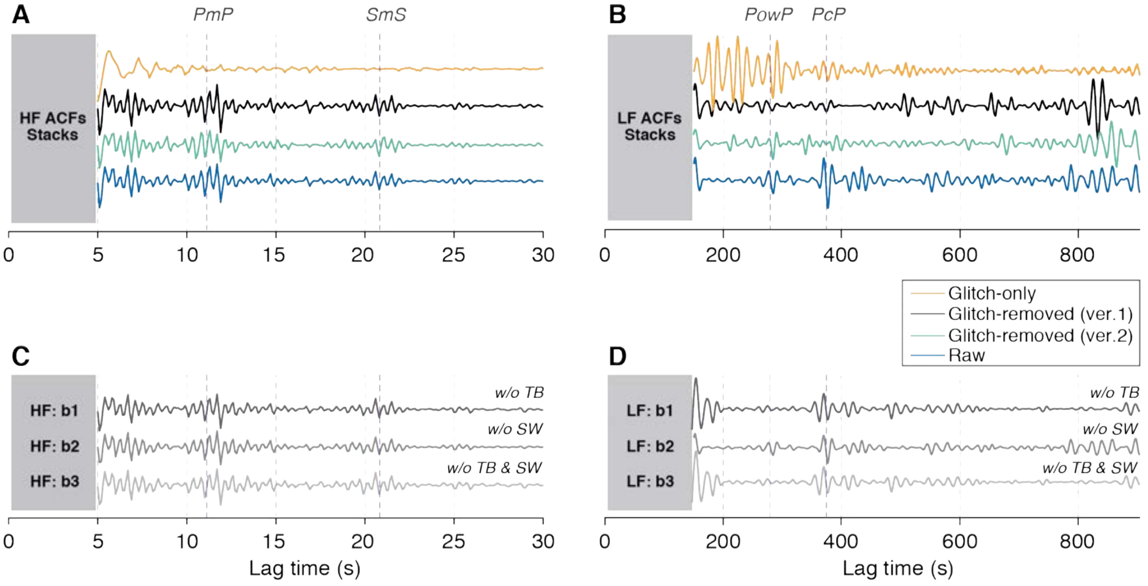

Figure 4. Comparison of the ACF stacks with different datasets obtained in our analysis. (A) Phase weighted stacks of HF and (B) LF ACFs based on 2-hour long raw vertical component data between February and July, 2019 (blue, Dataset 2), data with glitches identified and removed (black, Dataset 3), and data with only identified glitch signals (orange, Dataset 1). Each set of ACFs are computed following the data processing procedure in Deng and Levander (2020), so ACF stacks in blue are replicas of the ACFs shown in Deng and Levander (2020). The ACF stacks in green are similarly obtained using a different set of 2-hour long records between March and September, 2019 where glitches are removed by the procedure followed by Scholz et al. (2020). (C) Comparison of the phase weighted stacks of HF and (D) LF ACFs using the Dataset 1 omitting various normalization steps employed by Deng and

Levander (2020): temporal balancing (b1), spectral whitening (b2), and both (b3). Portions of the autocorrelation affected by source time function are grayed out. NB: Abbreviation on each trace in (C-D) denotes, TB = temporal balancing and SW = spectral whitening.

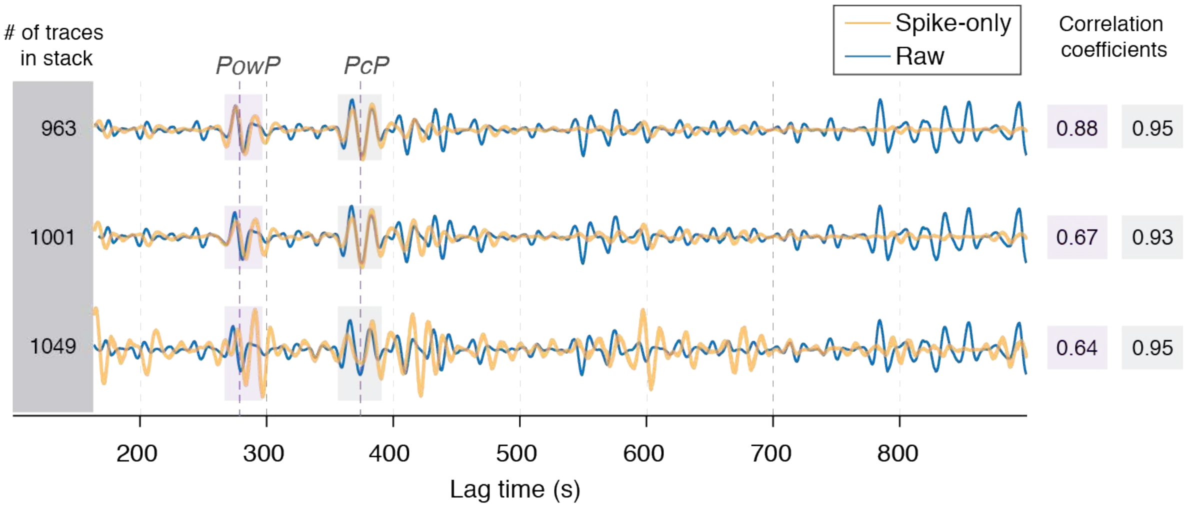

Figure 5. Effect of spikes in the ACF stacks.

Phase weighted stacks of LF ACFs based on 2-hour long vertical component data between February and July, 2019 (blue) compared to those computed using only signals of detected spikes (orange). Each set of ACFs is computed following the data processing procedure in Deng and Levander (2020). Spikes were detected in 1049 out of 1051 traces, and manually inspected to discard outliers, yielding spike-only ACFs with 1001 and 963 traces. Correlation coefficients between our spike-only LF ACF and DL LF ACF are computed around ~280s and ~375s phases (in shaded region) and shown on the right. Portions of the autocorrelation affected by source time function are grayed out.

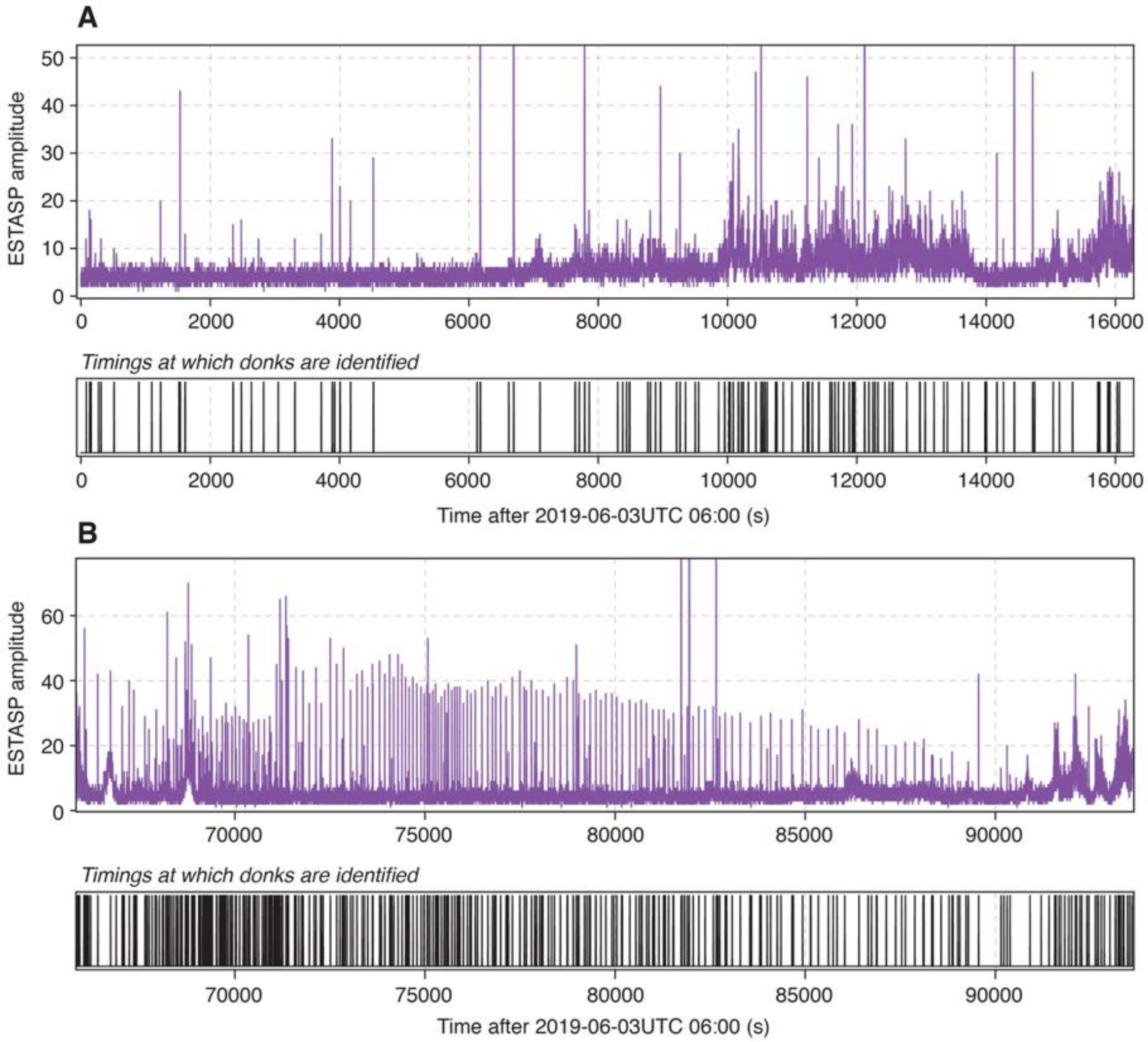

Figure 6. ESTASP amplitudes and distribution of the identified donks during quiet hours of Sol 184. ESTASP amplitudes and the timings associated with identified donks during the quiet hours of Sol 184, exclusively processed with data shown in Fig. 1F from (A) the first 16200s and (B) from 66000s to the end of the record. Donk signals are identified with a standard algorithm of STA/LTA a window length of 1s and 25s on each ESTASP channel. Data outside these time ranges are extremely noisy due to strong diurnal wind stresses hence it is difficult to verify the fidelity of identified donks and it requires a full span of complete SP data.

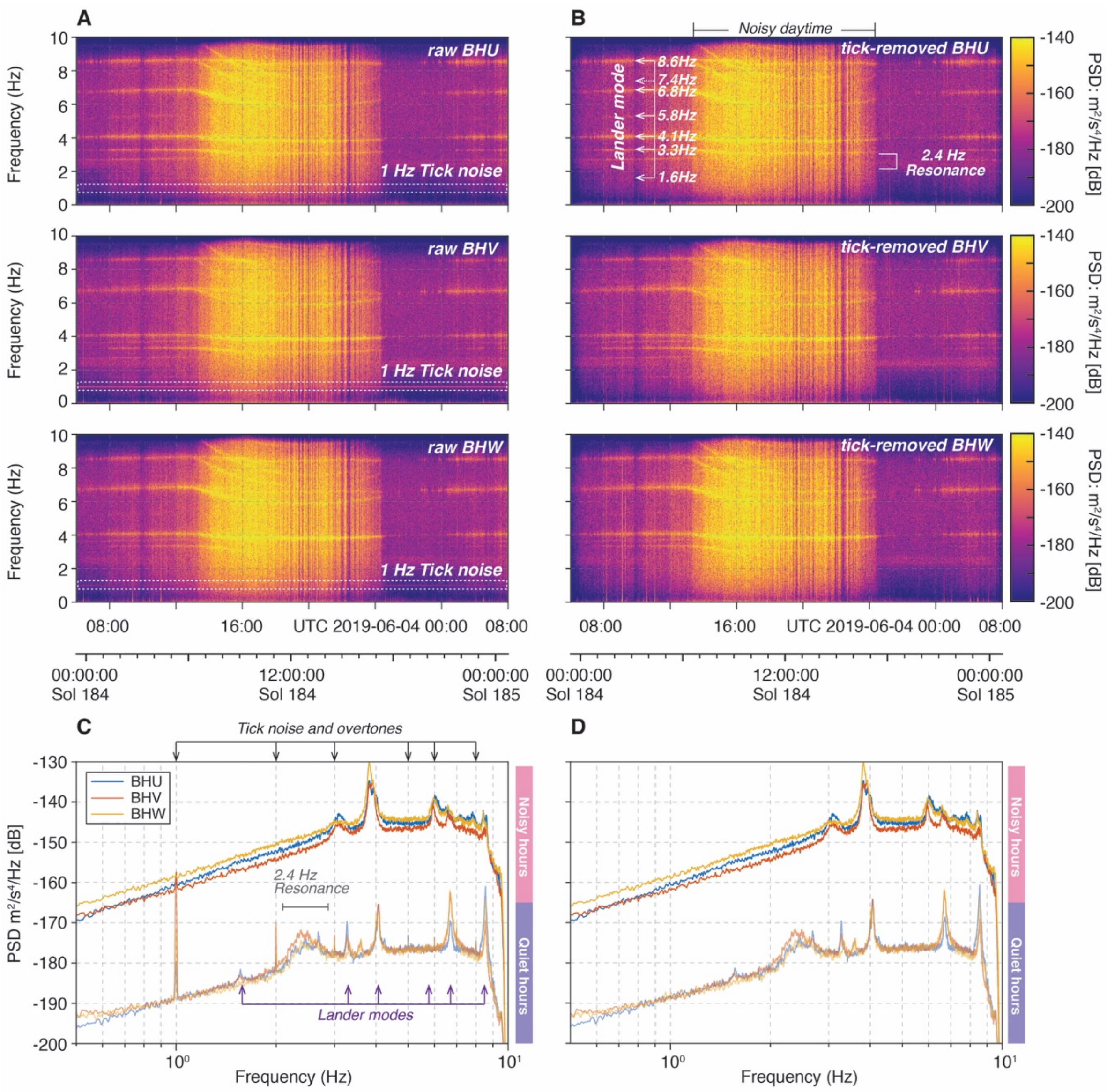

Figure 7. Comparison of the spectrograms of the ambient noise recording with and without the tick noise removal. (A) Spectrograms of the raw ambient noise data recorded on U, V, and W components during one day of Sol 184. White dashed box indicates observed tick noise at 1 Hz. (B) Same as (A) but after applying a tick noise removal procedure. For each channel, the tick noise waveform is estimated exclusively taking data recorded during the quiet hours (e.g., Fig. 1I) then subtracted from raw data following Compaire et al. (2021). (C) Comparison of the PSD for U, V, and W components during noisy vs. quiet hours. The tick noise at 1 Hz is strongly observed for both noisy and quiet hours. Notice during quiet hours however the corresponding harmonics are visible up to 6 Hz in the Sol 184 record. Given our understanding of the root cause of the tick noise we expect that these harmonics also exist above 10Hz. (D) Same as (C) but after applying a tick noise removal procedure described in Pitfall 4.

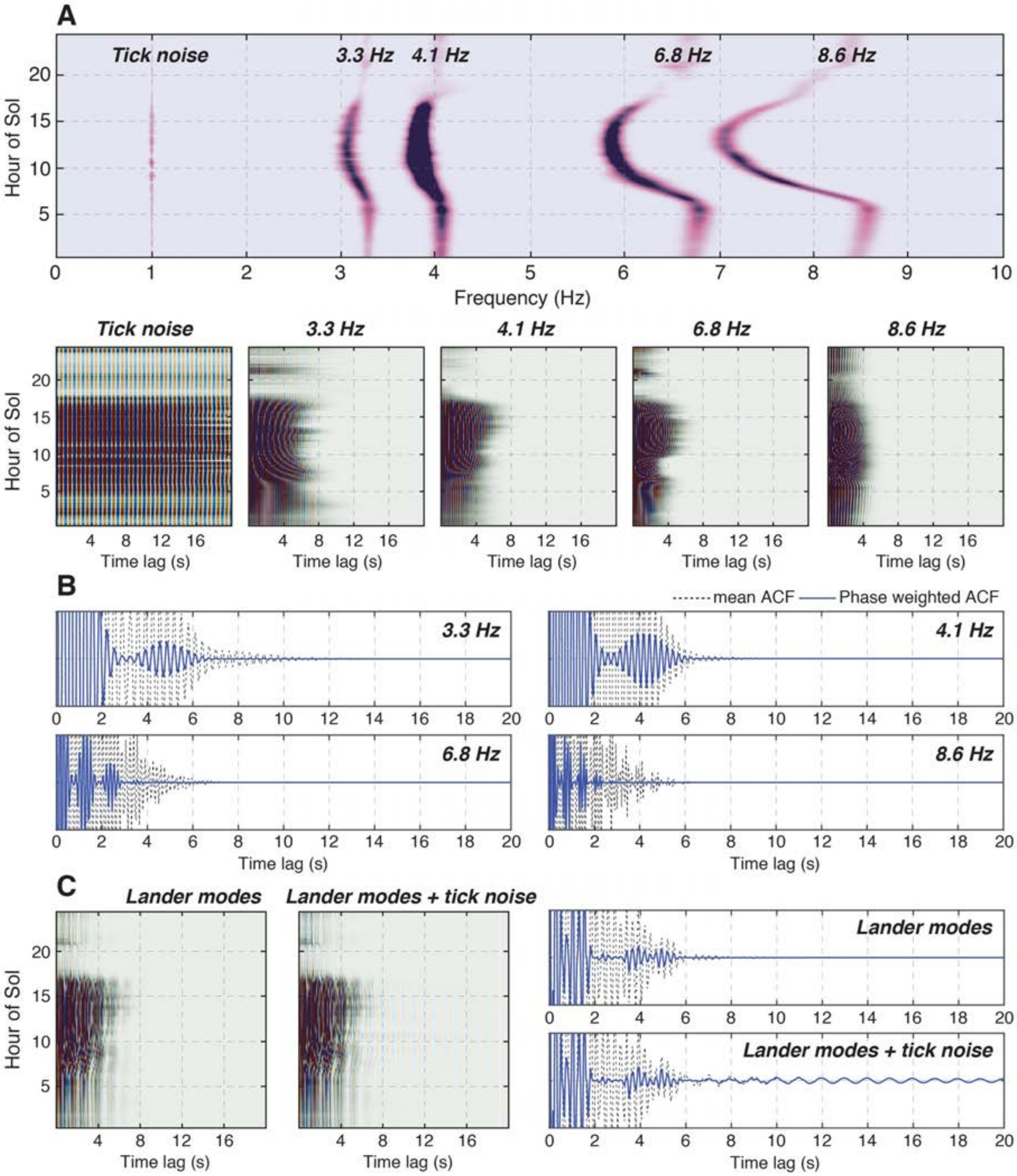

Figure 8. Identified lander modes and their effects on the ACFs. (A) Representative power spectra of the strongest lander modes (e.g., 3.3 Hz, 4.1 Hz, 6.8 Hz, and 8.6 Hz) including the tick noise at 1 Hz for the Martian Sol. Measurements of those lander mode frequencies, spectral widths and amplitudes are averaged for 7 Sols (185, 225,

345, 425, 505, 585, and 625) taking 70% overlapping 30-minute windows. Below, five panels show theoretical ACFs derived from summing the inverse Fourier transform of the representative power spectra for the tick noise and each solitary lander mode. (B) ACFs stacks for each lander mode shown in (A). Dashed black and solid blue traces indicate the mean and phase-weighted ACFs, respectively. (C) Same as (A-B) but incorporating all lander mode frequencies with and without the 1 Hz tick noise.

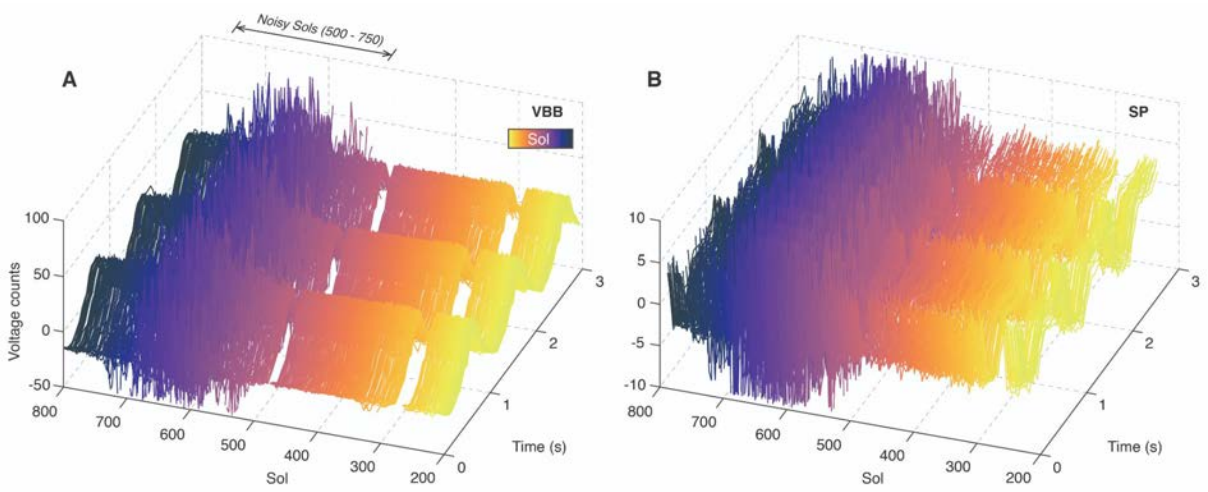

Figure 9. Overview of tick noise throughout the *InSight* seismic data. Tick noise, as obtained by stacking for each Sol the raw 20 sps data from 18:00 to 22:00 LMST on a 3s repeating window for (A) VBB-BHU and (B) SP1 records, yields the tick pattern repeating three times. Loss of the pattern between Sols 500 and 750 is due to the large amplitude ambient noise recorded during this period. Apart from that, the tick pattern is very consistent. Because the tick noise has an electromagnetic coupling origin, its amplitude in digital units is roughly proportional to the gain of the sensor feedback, which is much larger on the VBB than on the SP (Lognonné et al., 2019).

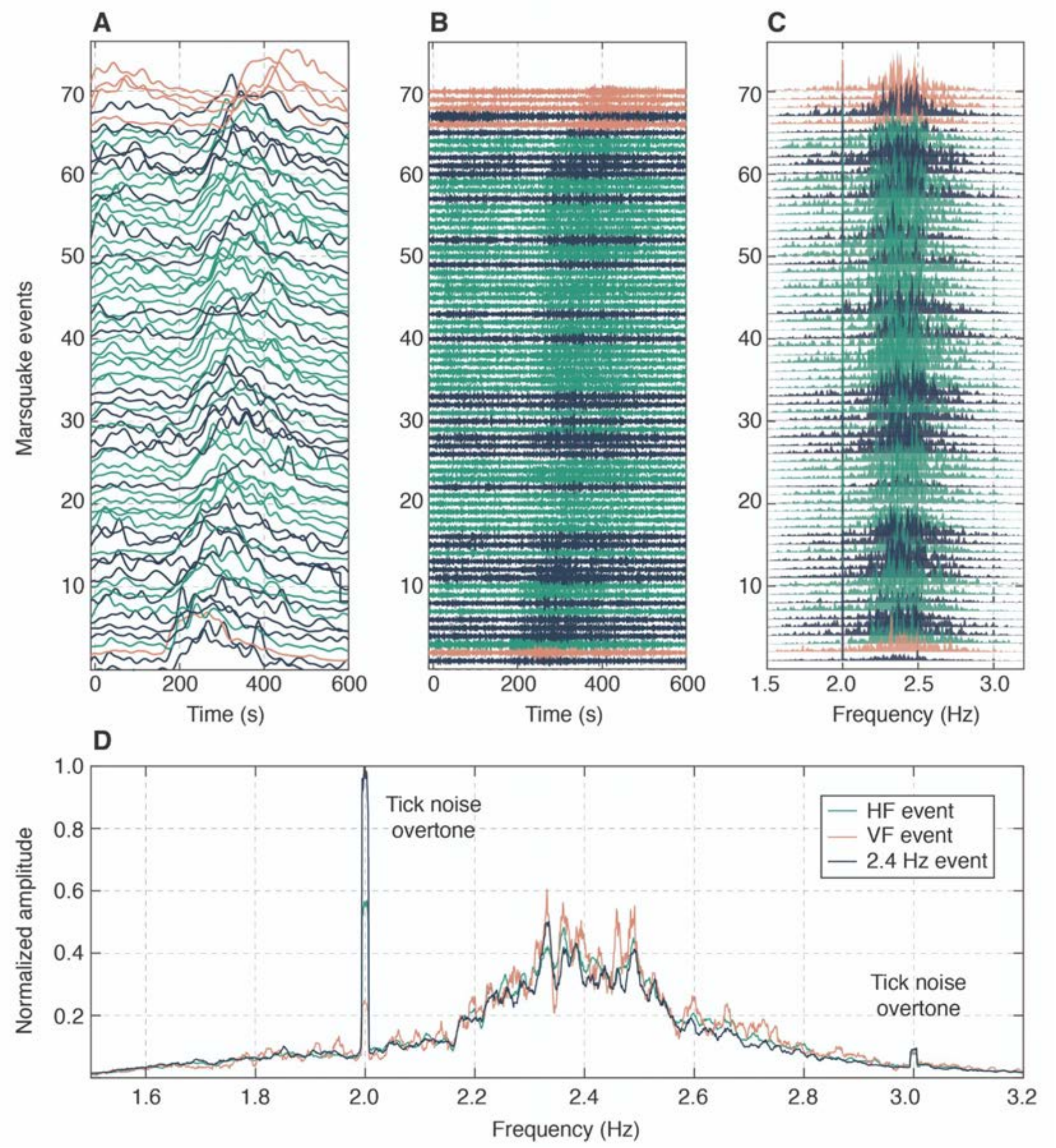

Figure 10. High frequency Marsquake waveforms and their corresponding normalized spectra. (A) Average three-component envelopes aligned on P-arrival (t = 0s) from a total of 70 marsquakes from the high frequency family that include high frequency (HF), very high frequency (VF), and the 2.4 Hz events, and the corresponding (B) vertical component waveforms. All MQS events with the event quality C or above are selected between Sol 128 and 500 (InSight Marsquake Service, 2021) but those with noticeable glitches in the analysis window are removed. For each event, we use a standard algorithm of STA/LTA triggering on the Hilbert envelope averaged across components to pick the Pg- and Sg-arrivals. Both envelopes and waveforms are sorted by the travel time between Sg and Pg picks. See van Driel et al. (2021) for more detailed analysis on these events. (C) Normalized amplitude spectra for each

individual event averaged across three-components and (D) the event sum based on different high frequency event types.

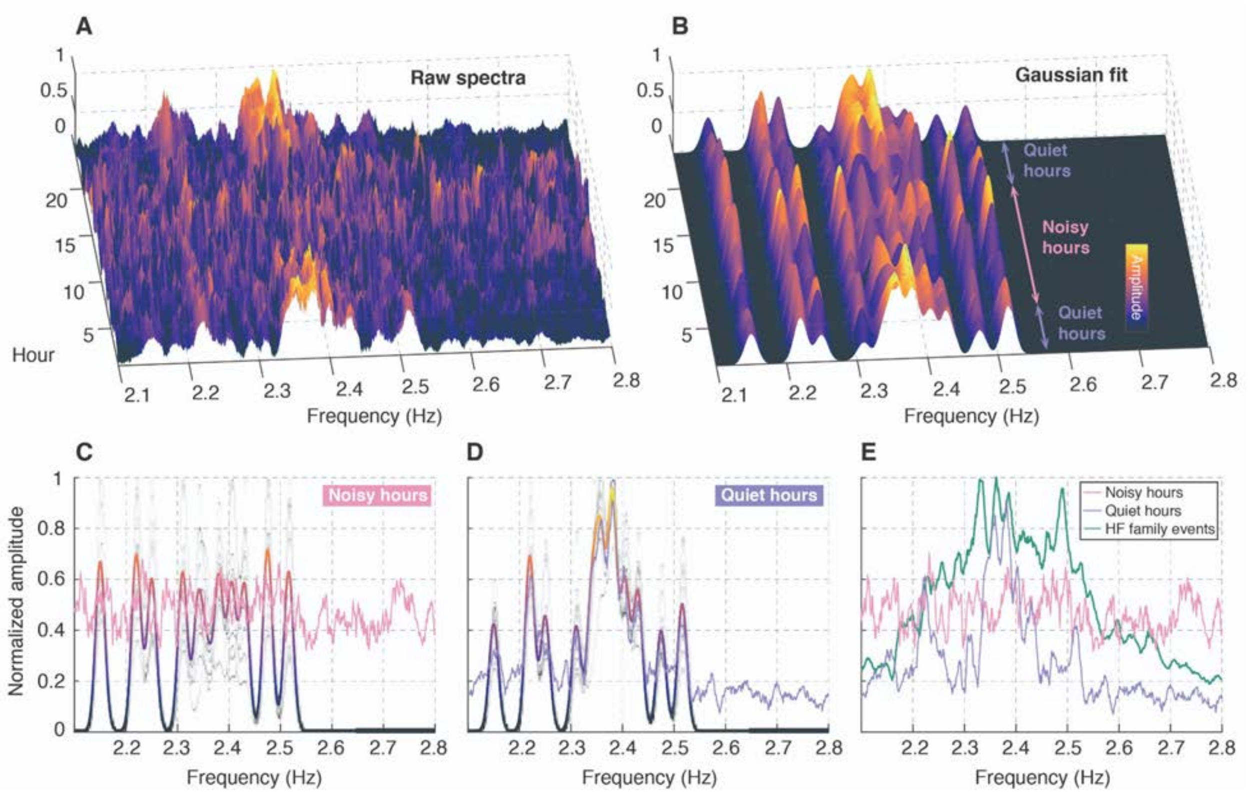

Figure 11. Hourly stacked ACFs and the 2.4 Hz resonance. (A) Normalized spectra of hourly summed SP ACFs using our glitch-removed records between February - July, 2019 (Dataset 2) and the corresponding (B) modeled spectra estimated by ten gaussian pulses whose central frequencies fit our data: 2.15 Hz, 2.22 Hz, 2.25 Hz, 2.31 Hz, 2.34 Hz, 2.38 Hz, 2.405 Hz, 2.43 Hz, 2.475 Hz, and 2.51 Hz. (C) Comparison of observed (line with a single color) vs. estimated mean spectra (line with the same color scheme used for (A-B)) of HF ACFs during noisy and (D) quiet hours during the Martian Sol. Gray lines indicate individual hourly spectra models in (B). (E) Observed mean spectra of HF ACFs (C-D) and the three-component average event sum in Fig. 10D.

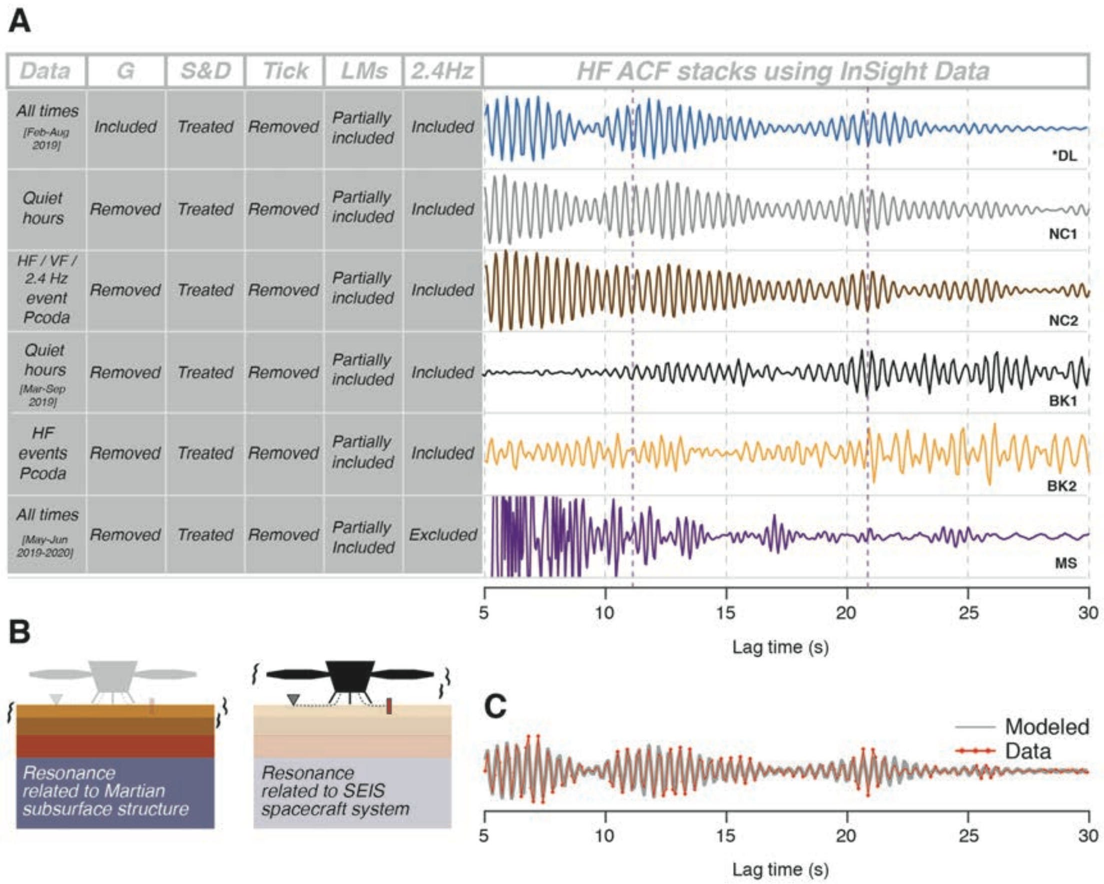

Data	G	S&D	Tick	LMs	2.4Hz	HF ACF stacks using InSight Data
All times [Feb-Aug 2019]	Included	Treated	Removed	Partially included	Included	*DL
Quiet hours	Removed	Treated	Removed	Partially included	Included	NC1
HF / VF / 2.4 Hz event Pcoda	Removed	Treated	Removed	Partially included	Included	NC2
Quiet hours [Mar-Sep 2019]	Removed	Treated	Removed	Partially included	Included	BK1
HF events Pcoda	Removed	Treated	Removed	Partially included	Included	BK2
All times [May-Jun 2019-2020]	Removed	Treated	Removed	Partially Included	Excluded	MS

Figure 12. Comparison of the HF ACF stacks in the literature and structural implications. (A) The HF ACF stacks produced by various author groups in the literature. The first 5s of data is removed due to various source effects. For each ACF, the five Pitfalls discussed in the main text are either removed or treated differently prior to autocorrelation. NB: Labels used as table headers denote, G = Glitches; S & D = Spikes and Donks; Tick = Tick noise; LMs = Lander modes; 2.4 Hz = the 2.4 Hz resonance. Labels used for HF ACFs denote, *DL = the replicated HF ACF stack followed by Deng and Levander (2020) bandpass filtered between 1- 3 Hz; NC1 = ambient noise HF ACF stack and NC2 = HF event family coda ACF stack in Compaire et al. (2021); BK1 = ambient noise HF ACF stack and BK2 = HF event coda ACF stack in Knapmeyer-Endrun et al. (2021) (see traces labeled as C3 and C1 in Fig. 3); MS = HF ACF stack in Schimmel et al. (2021). (B) Two main working hypotheses on the origin of the 2.4 Hz resonance visible in the ACFs: resonance generated by a subsurface structure of Mars and/or another unexplained mode related to the lander. (C) Modeled ACF synthesized by summing nine decaying cosine functions whose frequencies correspond to the spectral peaks observed in the 2.4 Hz resonance in Fig. 10 decaying with a single attenuation parameter. ACF data (red) behind the synthetic ACF is the same plotted as blue trace in (A).